

# **Structural and Electronic properties of Titanium doped $\text{LaNiO}_3$ thin films**

**M.Sc. Thesis**

By

**Sourav Singh Tomar**



**DISCIPLINE OF PHYSICS  
INDIAN INSTITUTE OF TECHNOLOGY INDORE**

**JUNE 2020**

# **Structural and Electronic properties of Titanium doped $\text{LaNiO}_3$ thin films**

**A THESIS**

*Submitted in partial fulfilment of the  
requirements for the award of the degree  
of  
Master of Science*

*By*

**Sourav Singh Tomar**



**DISCIPLINE OF PHYSICS  
INDIAN INSTITUTE OF TECHNOLOGY INDORE  
JUNE 2020**



## INDIAN INSTITUTE OF TECHNOLOGY, INDORE

### CANDIDATE'S DECLARATION

I hereby that the work presented in the thesis entitled '**Structural and Electronic properties of Titanium doped LaNiO<sub>3</sub> thin films**' in the partial fulfilment of the requirements for the award of the degree of **MASTER OF SCIENCE** and submitted in the **DISCIPLINE OF PHYSICS, INDIAN INSTITUTE OF TECHNOLOGY INDORE**, is an authentic record of my work carried out during the time period from July 2018 to June 2020, under the supervision of Dr. Krushna R. Mavani, Professor, Discipline of Physics, Indian Institute of Technology Indore.

The matter presented in this thesis has not been submitted by me for the award of any other degree of this or any other institute.

**Signature of the student**  
**Sourav Singh Tomar**

---

This is to certify that above statement made by the candidate is correct to the best of my knowledge.

**Signature of Supervisor**  
**Dr. Krushna R. Mavani**

---

**Sourav Singh Tomar** has given his M.Sc. Oral Examination on 24-06-2020

**Signature of supervisor of thesis**

**Date- 07/07/2020**

**Signature of PSPC member #1**

**Convener, DPGC**

**Date- 07/07/2020**

**DEDICATED TO  
MY PARENTS AND TEACHERS**

## ACKNOWLEDGMENTS

It is not possible to mention all the people who have been supporting me during the two year journey of my stay at IIT INDORE, but I would like to enumerate a few of them.

First and foremost, I would like to pay my special gratitude to my thesis supervisor Dr. Krushna R. Mavani, Professor, Department of Physics, Indian Institute of Technology, Indore for giving me opportunity to work in PLD lab. She supported me throughout my project. She guided me to approach a research problem. Her immense knowledge, constant encouragement and logical approach helped me a lot to build up a basis for present thesis. I would also like to thank my PSPC members Dr. Sudeshna Chattopadhyay and Dr. Srimanta Pakhira for their valuable suggestions.

I like to thank my lab members for their support throughout the project duration. Their encouragement, suggestions and support help me a lot during this journey. I specially want to mention Ms. Ekta Yadav who helped me in sample preparation, characterization and data analysis. She also gives me moral support during this project. I thank Mr. Harisankar S., Mr. Ankit Soni, Mrs. Kavita Soni, Ms. Komal Mulchandani, Ms. Komal Pathy and Mr. Shubham Kothari for their support during whole year.

I would like to thank all the faculty members and the staff members of the Physics Discipline IIT, Indore for their help and support.

I would like to pay my sincere regards to all my friends in IIT Indore with whom I enjoy this phase of my life. Lastly, my life is indebted to my parents and sisters for their love, support and understanding.

## Abstract

Perovskite oxides exhibit lot of practical applications that make them a potential candidate for physics now a days. Rare earth nickelates  $RNiO_3$  show phase transition, strongly correlated effects, Colossal Magnetoresistance, high temperature superconductivity *etc.* All these properties are highly controllable in thin film form. In the phase diagram of  $RNiO_3$ ,  $LaNiO_3$  does not show metal to insulator transition. We have deposited thin films of  $LaNi_{1-x}Ti_xO_3$  ( $x=0-0.10$ ) on  $LaAlO_3$  (001) (LAO) single crystal substrate using pulsed laser deposition method and studied the effect of Ti doping on structural and electronic properties. All the films are highly oriented towards the (001) substrate axis. The resistivity measurements indicate that the films remains metallic even at low temperature range and there is no metal to insulator transition observed. Although, the resistivity of the system increases with doping. The power law fitting of resistivity data shows the non-Fermi behaviour of the system. With doping, blue-shift of Raman modes is observed that indicates change in Ni-O-Ni bond angle and  $NiO_6$  octahedra distortion. Temperature dependent Raman spectroscopy show the red shift in all the thin films. It helps to study the effects of Ti doping on the structural and electronic properties of  $LaNiO_3$ .

## **Publication**

*Systematic effects of Ti doping on the electronic properties of LaNiO<sub>3</sub> thin films.*

**Sourav Singh Tomar**, Ekta Yadav, Kavita Soni, K R Mavani, *Bulletin of Materials Science* (SUBMITTED)

# TABLE OF CONTENTS

LIST OF FIGURES \_\_\_\_\_

LIST OF TABLES \_\_\_\_\_

## Title

### Chapter 1: INTRODUCTION

- 1.1 Introduction to complex oxides.
- 1.2 Jahn-Teller Effect
- 1.3 Electrical Transport
  - 1.3.1 Free Electron Theory
  - 1.3.2 Band Theory of Solids
  - 1.3.3
  - 1.3.4 Mott Hubbard Theory
  - 1.3.5 Zaanen-Sawatzky-Allen model
  - 1.3.6 Non-Fermi Liquid Theory
- 1.4 Rare Earth Nickelates
- 1.5 Motivation

### Chapter 2: Experimental Techniques

- 2.1 Sample Preparation
  - 2.1.1 Bulk Target Synthesis
  - 2.1.2 Thin Film Synthesis using PLD
- 2.2 Characterization Techniques
  - 2.2.1 X-Ray Diffraction (XRD)
  - 2.2.2 Temperature dependent resistivity measurement
  - 2.2.3 Raman Spectroscopy

## **Chapter 3: Results and Discussion**

3.1 XRD analysis of  $\text{LaNi}_{1-x}\text{Ti}_x\text{O}_3$  ( $x=0-0.10$ ) thin films on LAO substrate

3.2 Temperature Dependent Resistivity Measurement of  $\text{LaNi}_{1-x}\text{Ti}_x\text{O}_3$  ( $x=0-0.10$ ) thin films on LAO substrate

3.3 Raman Spectroscopy of  $\text{LaNi}_{1-x}\text{Ti}_x\text{O}_3$  ( $x=0-0.10$ ) thin films on LAO substrate

3.3.1 Room Temperature Raman Spectroscopy

3.3.2 Temperature dependent Raman Spectroscopy

3.4 Conclusion.

## **References.**

## LIST OF FIGURES

<b>Figure</b>	<b>Caption</b>
Fig. 1.1	Ideal cubic perovskite structure
Fig. 1.2	Crystal field splitting and John-teller distortion of 3d orbital
Fig. 1.3	Schematic of potential well for free electron with infinite potential at surface and zero otherwise.
Fig. 1.4	Schematic of bands in insulator, semiconductor and metals.
Fig. 1.5	Schematic structure of an insulator and a metal. E and $E_f$ stands for Energy and Fermi Energy respectively.
Fig. 1.6	Schematic of ZSA framework.
Fig. 1.7	Mott-Hubbard and Charge-transfer insulator.
Fig. 1.8	Phase Diagram of $RNiO_3$ compounds.
Fig. 2.1	Schematic of Pulsed laser Deposition Set-up.
Fig. 2.2	Schematic of X-Ray Diffraction set-up.
Fig. 2.3	Film showing Tensile strain.
Fig. 2.4	Film showing Compressive strain.
Fig. 2.5	Four probe set-up.
Fig. 2.6	Schematic representation of Rayleigh and Raman Scattering.
Fig. 2.7	Schematic diagram of Raman spectroscope.
Fig. 3.1	X-ray diffraction of $LaNi_{1-x}Ti_xO_3$ ( $x=0-0.10$ ) thin films grown on LAO (001) substrate.
Fig. 3.2	Enlarge view of (002) Bragg diffraction of $LaNi_{1-x}Ti_xO_3$ ( $x=0-0.10$ ) thin films.
Fig. 3.3	Resistivity vs temperature plots for $LaNi_{1-x}Ti_xO_3$ ( $x=0.0-0.10$ ) thin films on LAO (001). The inset figure shows resistivity vs doping at room temperature (300 K) and 15 K.

Fig. 3.4 Resistivity vs temperature plots for  $\text{LaNi}_{1-x}\text{Ti}_x\text{O}_3$  ( $x=0.0-0.10$ ) thin films on LAO (001). The red line shows fitting of resistivity using power law equation

Fig. 3.5 Room temperature Raman Spectra of  $\text{LaNi}_{1-x}\text{Ti}_x\text{O}_3$  ( $x=0.0-0.10$ ) thin films.

Fig. 3.6 Percentage Doping of Ti vs FWHM and Raman Shift of  $\text{LaNi}_{1-x}\text{Ti}_x\text{O}_3$  ( $x=0.0-0.10$ ) thin films.

Fig. 3.7 Temperature dependent Raman spectroscopy of  $\text{LaNi}_{1-x}\text{Ti}_x\text{O}_3$  ( $x=0.0-0.10$ ) thin films.

## **LIST OF TABLES**

Table 1- Parameters of PLD at the time of deposition.

Table.2- Transport properties of  $\text{LaNi}_{1-x}\text{Ti}_x\text{O}_3$  ( $x=0-0.10$ ) thin films deposited on LAO.

Table.3 - Fitting parameters of FWHM and Raman Shift shown in Fig-3.6.



# Chapter 1-INTRODUCTION

## 1.1 Introduction to complex oxides

Reducing the size and the enhancement in practical applications of appliances are the requirements of today's technology that will replace the old Silicon based technology [1,2]. Nanomaterials, thin films and their fabrication, and oxides are most suitable replacement choices. A layer of material which has thickness in several nanometres is known as thin film. Island growth, layer by layer growth, and mixed growth are different type of thin film growth techniques. Thin films have wide range of applications like in electronic and switching devices, optical electronics etc [2,3]. Transition metal oxides (complex oxides) act as the most suitable material for these applications. In last few decades, Rare earth cuprates ( $\text{RCuO}_3$ ), rare earth nickelates ( $\text{RNiO}_3$ ), and rare earth manganites ( $\text{RMnO}_3$ ) are most studied complex oxides because of high temperature superconductivity, Colossal Magnetoresistance, Giant Magnetoresistance respectively [4]. In addition to this, reduction in dimensionality in thin films and heterostructure have increased the interest of researchers in this field.

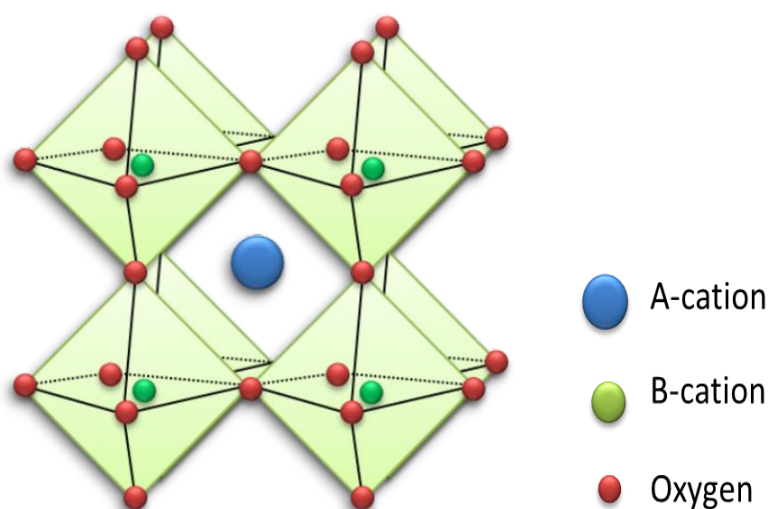


*Fig.1.1-Ideal cubic perovskite structure*

Perovskite oxides have general formula  $\text{ABO}_3$ , where A and B are cations. A site is occupied by larger ions of rare earth, alkali or alkaline earth metal whereas B site is occupied by smaller ions of transition metals. Ideally, a perovskite has a cubic unit cell with B-O-B bond angle  $180^\circ$  with one A cation surrounded by eight  $\text{BO}_6$  octahedra, as shown in Fig-1.1. Stability of structure is determined by the tolerance factor that is defined by:

$$t = \frac{(R_A + R_B)}{\sqrt{2}(R_B + R_O)} \quad \text{-----} 1.1$$

Where  $R_A$ ,  $R_B$  and  $R_O$  are the radii of A, B and oxygen (O) ions, respectively. Generally, value of  $t$  lies between 0.75 to 1 [5].

For the ideal cubic structure, the value of the tolerance factor should be 1 [6]. For that purpose, A ion radius should be large. Any change in radius of ion A can cause distortion in  $BO_6$  octahedra and create instability. This is commonly, known as orthorhombic distortion. Many oxides form perovskite structure. The lattice degrees of freedom of this perovskite structure allows accommodation to various dopants at A and B sites, thereby provides a platform for modifications in properties through chemical variation[7].

### **1.2-Jahn Teller Effect**

Transition oxides experience geometrical distortion too. If, for an electron, more than one energy state is available with same energy *i.e.* degenerate states then energy cost for electronic configuration is higher. To reduce this energy cost, the structure undergoes a distortion and takes the system to lower energy state. Due to crystal field splitting in octahedral environment, degenerated five d orbitals split in two  $e_g$  and three  $t_{2g}$  orbitals. The last electron of metal ions having configuration  $d^1$ ,  $d^2$ ,  $d^4$ ,  $d^6$ ,  $d^7$  and  $d^9$  has more than one free state to acquire. This state of dilemma for last electron can be avoided by either compressing or elongating the  $BO_6$  in a way that energy of some orbitals become lower than others. This compression along Z axis is known as z-in distortion and elongation along Z axis is known as z-out distortion. This effect is known as **Jahn Teller Effect** [8,9]. As the electronic and magnetic properties of these  $ABO_3$  perovskite depends on B-O-B bond angle and bond length, so Jahn teller distortion plays an important role in determining the properties of perovskite oxides.

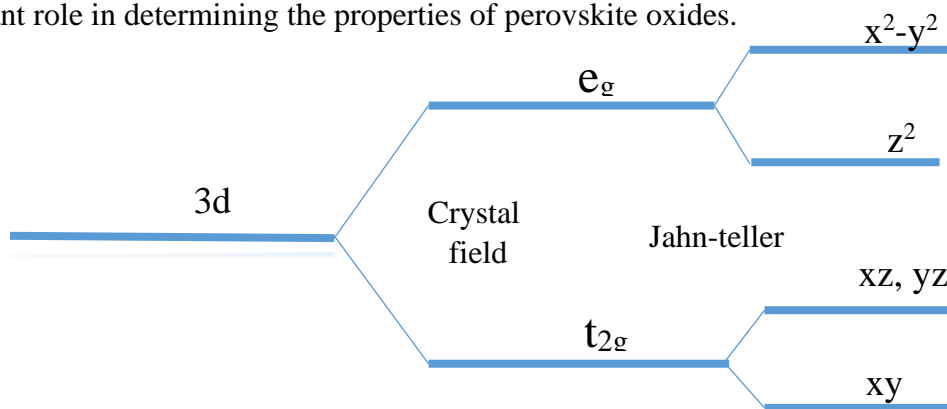


**Fig.1.2- Crystal field splitting and John-teller distortion of 3d orbital**

## **1.3-Electrical Transport:**

Electric transport is described by the passing of current in a material. The higher the electrical conductivity ( $\sigma$ ), the easier the motion of electron in the material. Materials are broadly divided into metal and insulator. For metal, electrical conductivity is of the order of  $10^9 \Omega^{-1}\text{cm}^{-1}$  and for insulator, it is  $10^{-20} \Omega^{-1}\text{cm}^{-1}$ . At 0 K, insulators show zero conductivity while metals have a finite conductivity. As temperature increases, the resistivity ( $\rho$ ) of the insulator decreases *i.e.*  $d\rho/dT < 0$ , while for metal resistivity increases with temperature *i.e.*  $d\rho/dT > 0$ .

Oxides show large difference in electrical behaviour. There are many theories which distinguish between metal and insulator [10]. Some of these are as follows:

### **1.3.1-Free Electron Theory:**

The free electron model (basically for metals) was given by Paul Drude [11]. In this model, the electrons in the metal are considered as free gas particles that are non-interacting. The potential at the surface of the solid is only potential they experience. These are the few assumptions while formulating this electron;

- a) Electrons do not interact among themselves.
- b) All positive ions are immobile because of their large mass.
- c) Electrons are free to move inside metals,
- d) Electrons undergo instantaneous collision with positive ions.

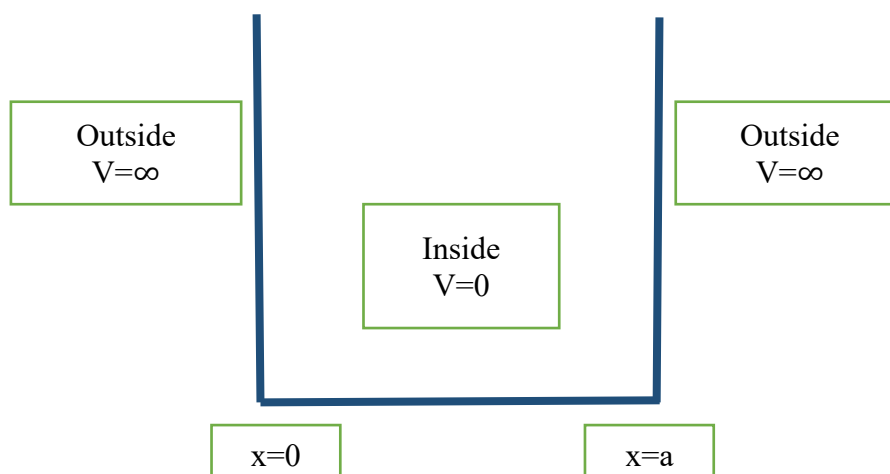


***Fig.1.3-Schematic of potential well for free electron with infinite potential at surface and zero otherwise.***

In presence of electric field, the electrical conductivity  $\rho$  is given by

$$\rho = \frac{m}{n\tau e^2} \quad \text{-----1.2}$$

where,  $n$  is free electron density,  $e$  is electron charge,  $\tau$  is relaxation time, and  $m$  is electron mass.

This theory successfully explains ohm's law, electrical conductivity, thermal conductivity and Hall Effect. However, it could not explain sign of Hall coefficient for some metals, heat capacity, temperature dependent resistivity *etc.* It also could not distinguish between metals and insulators.

### **1.3.2-Band Theory of Solids:**

The assumption of ignoring the interaction between positive ions and electron was the main reason of free electron theory failure. Actually, we cannot ignore the potential field due to positive ions. According to the band theory, electrons in solid experience periodic potential due to ions at the lattice point. However, electron-electron interaction is not considered in this model. The periodic potential of positive ions is given by:

$$V(x + a) = V(x) \quad \text{-----1.3}$$

Where,  $a$  is lattice constant. The Kroning-Penny model assumes this potential as periodic box potential. The 1-D Schrödinger equation for an electron in this periodic potential is given by:

$$\left[ \frac{-\hbar^2}{8m\pi^2} \frac{d^2}{dx^2} + V(x) \right] \Psi(x) = E\Psi(x) \quad \text{-----1.4}$$

In accordance of Bloch theorem, the solution of this equation is given by:

$$\Psi(x) = e^{ik \cdot x} u_k(x) \quad \text{-----1.5}$$

Where,  $k$  is wave vector and  $u_k(x)$  is periodic wave function.

The relation between energy  $E$  and wave vector  $k$  comes out as

$$\cos(ka) = \cos(\alpha a) + P \frac{\sin(\alpha a)}{\alpha a} \quad \text{-----1.6}$$

Where,  $\alpha^2 = \frac{8\pi^2mE}{h^2}$  and  $P = \frac{4\pi^2mVba}{h^2}$  are constants with b as barrier width and a as lattice period.

The equation 1.6 suggests constraint on the occupancy of energy states as  $\cos(\mathbf{ka})$  has values between -1 and 1. It means that there are some energy regions where the solutions for the wave function are not possible. These regions are known as forbidden energy regions or band gaps. Depending on these band gaps, materials are classified in three categories. Metals that do not have any band gap, semiconductors that have small band gaps and insulators which have large band gaps at room temperature. These are shown in fig 1.4.

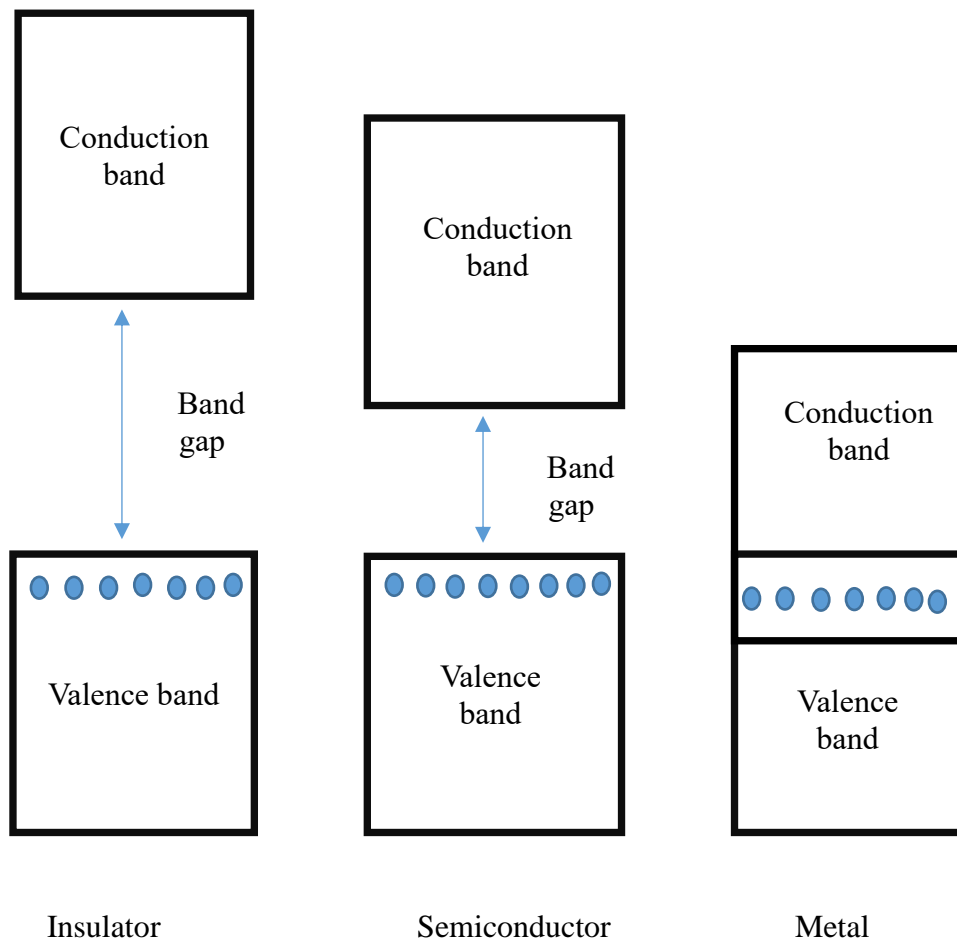


*Fig1.4- Schematic of bands in insulator, semiconductor and metals*

### 1.3.3-Mott-Hubbard model

As Band Theory did not account electron-electron interaction, it could not explain insulating state in some oxides of transition metal [12]. This model considers the coulomb interaction between electrons. The Hubbard Hamiltonian includes two parts, one is kinetic energy term and second is coulomb repulsive term. This Hamiltonian is given by

$$H = -t\sum_{\langle i,j \rangle, \sigma} (C_{i,\sigma}^+ C_{j,\sigma} + hc) + U\sum_{i=1}^N n_i n_j \quad \text{-----1.7}$$

where  $t$  is hopping integral,  $C_{i,\sigma}^+$  and  $C_{j,\sigma}$  are annihilation and creation operators respectively and  $U$  is the on-site coulomb interaction energy and is the energy cost of putting two electrons at one site, that is allowed by Pauli's Exclusive Principle [13]. The energy cost is large in strongly correlated oxides that results in splitting of  $d$  orbitals in two bands. The lower band is called Lower Hubbard band (LHB) and is fully filled and upper band is called Upper Hubbard band (UHB) and is empty. The strength of electron correlation is measured by the  $U/t$  parameter that determines conducting state of material [14]. For metals,  $U/t \ll 1$  that means the on-site coulomb repulsion is negligible and for insulators,  $U/t \gg 1$  that means the on-site coulomb repulsion is strong. These insulators are known as Mott-Hubbard insulators. Fig 1.5 describes it.

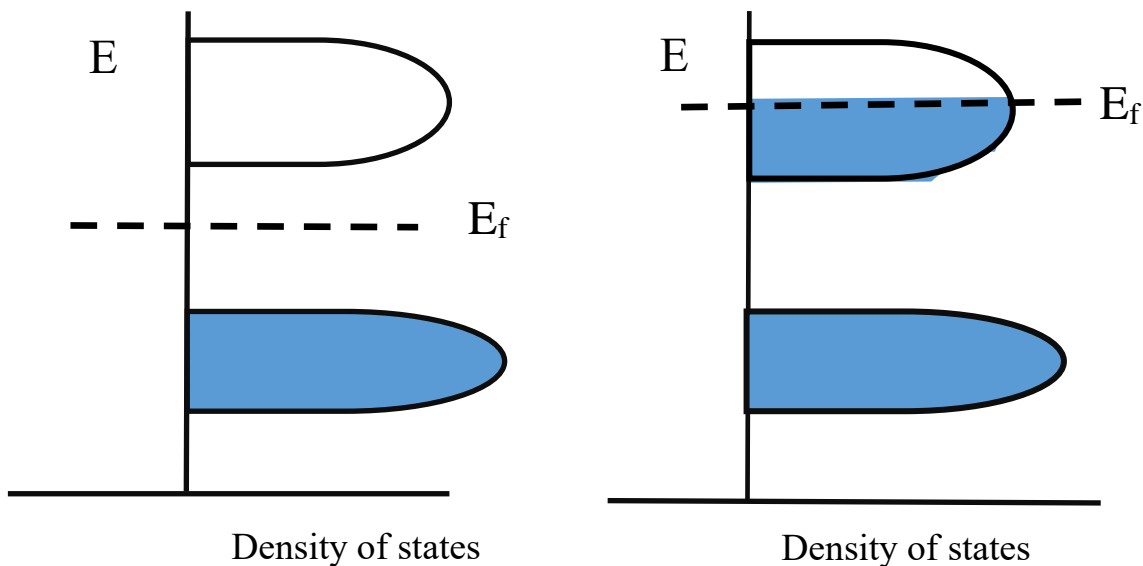


**Fig1.5- Schematic structure of an insulator and a metal.  $E$  and  $E_f$  stands for Energy and Fermi Energy respectively**

Mott-Hubbard model explains the insulating characteristic of many transitions metal oxides but it could not explain some sulphides metallic character [15].

### 1.3.4-Zaanen-Sawatzky-Allen model

This model depends on three parameters:

- i) Coulomb repulsion energy ( $U$ )
- ii) Band width ( $W$ )
- iii) Charge transfer gap ( $\Delta$ )

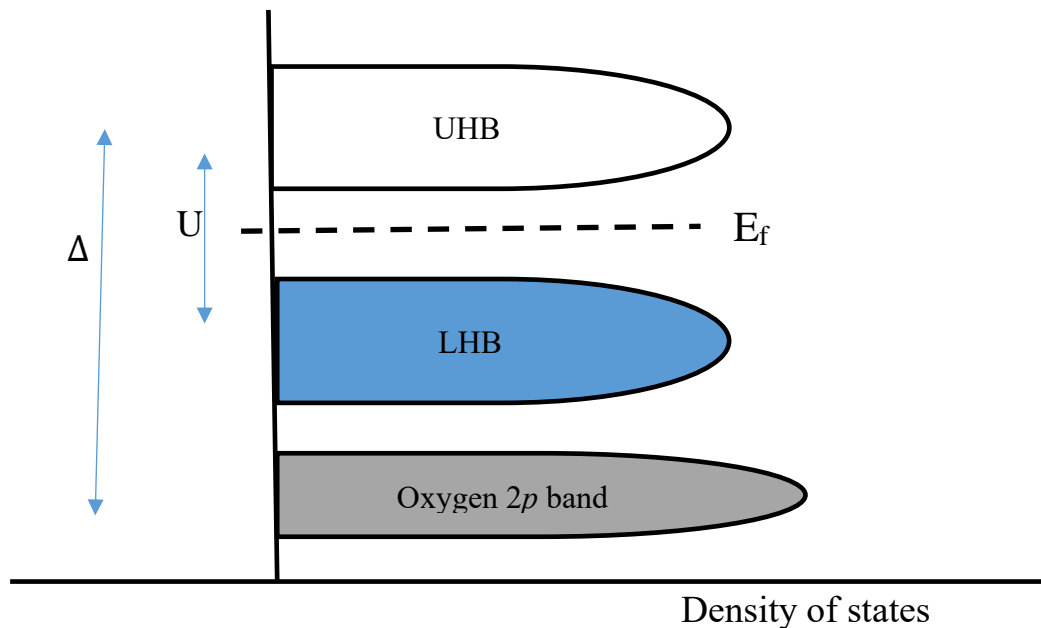


**Fig.1.6- Schematic of ZSA framework**

Here,  $\Delta$  is the difference in energy between 2p band of the anion and unoccupied 3d band of transition metal ion,  $U$  is the difference in energy between LHB and UHB of the transition metal ion and  $W$  is the band width of these of the Hubbard bands as shown in Fig.1.6. According to this model band gap is either of  $U$  or  $\Delta$ , depending whichever has lower size of energy scale [16]. So, insulators can be divided in two types.

- a) When  $W < U < \Delta$  *i.e.* difference in energy between LHB and UHB is less than that of 2p band of anion and UHB, then conduction will take place between LHB and UHB. These are called Mott Insulators as shown in Fig-1.7.
- b) When  $W < \Delta < U$  *i.e.* difference in energy between LHB and UHB is more than that of 2p band of anion and UHB, then conduction will take place between 2p band of anion and UHB. These are called Charge-transfer Insulators as shown in Fig 1.7.



Fermi Liquid (NFL) state. The NFL behaviour indicates the presence of degrees of freedom beyond the electrons themselves and are often associated with quantum critical behaviour [18]. In NFL system, three values of  $n$  (1, 1.3, and 1.6) are reported. The equation 1.8 fits only in certain range of temperature. So, to describe the resistivity behaviour of the system completely, resistivity saturation has to be considered [16-18]. It is given by:

$$\rho^{-1}(T) = \rho^{-1}_{\text{NFL}}(T) + \rho^{-1}_s \quad \text{-----1.9}$$

where  $\rho_s$  is resistivity saturation and acts as a parallel resistor. It is often related to maximum resistivity that approaches the limit of Mott-Ioffe-Regel (MIR) in certain cases [17].

$$\rho_{\text{MIR}} = \frac{3\pi^2\hbar}{q^2k_F^2l_m} \quad \text{-----1.10}$$

Here,  $l_m$  is the minimum mean free path.

#### **1.4-Rare earth nickelates:**

Rare earth nickelates have general formula  $\text{RNiO}_3$ . These compounds show first order metal to insulator transition (MIT) and are widely used in making electronic switches, electrical oscillators, thermal sensors, chemical sensors *etc.* [6,7]. By varying certain parameters like temperature, strain, doping, pressure etc, the electronic transition of these compound can be tuned [21]. Fig 1.8 shows the phase diagram of  $\text{RNiO}_3$  compounds.

From the phase diagram, we can observe that all the rare earth nickelates  $\text{RNiO}_3$  show first order metal to insulator transition except  $\text{LaNiO}_3$  [19,20]. By changing the size of rare earth ion, metal to insulator transition temperature *i.e.*  $T_{\text{MI}}$  changes. The structure of these compounds also changes because of the variation of the packing fraction with rare earth ion size. In  $\text{RNiO}_3$  family,  $\text{LaNiO}_3$  (LNO) shows paramagnetic-metallic state throughout the temperature range (12K- 300K) and does not show any metal to insulator transition. Although, other compounds shows metal to insulator transition with temperature [19,20].

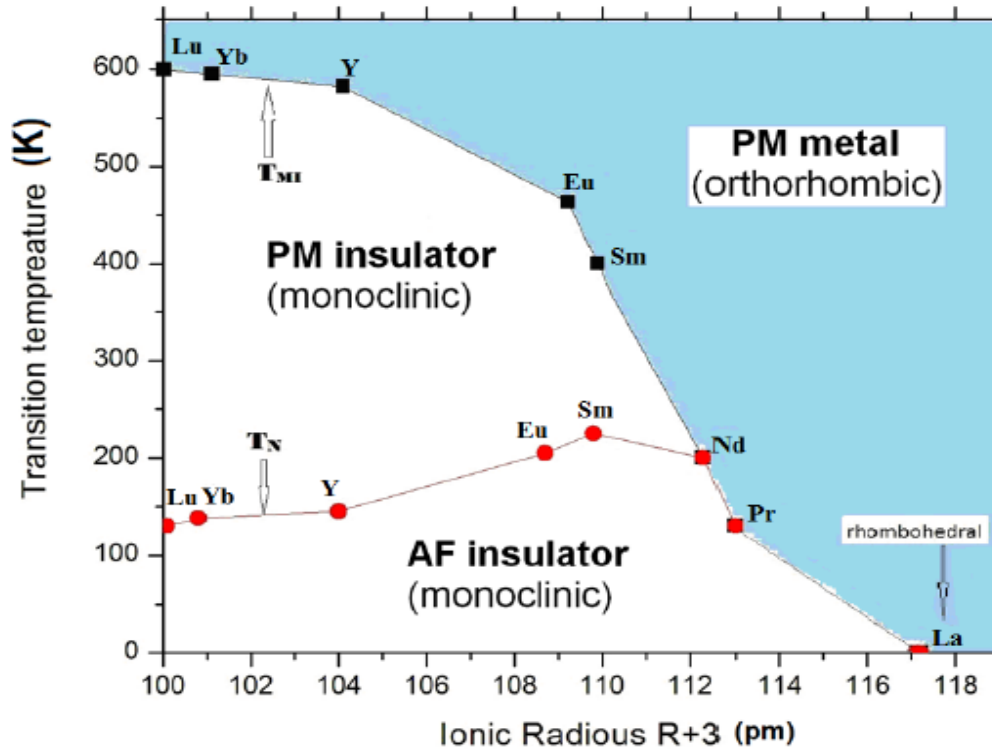


**Fig.1.8- Phase Diagram of RNiO<sub>3</sub> compounds**

In bulk, it is difficult to synthesis LNO in pure form [22] but with the advancement of thin film deposition techniques, thin films can be synthesised easily. The LNO thin films have wide range of applications in electrode devices, thermal and gas sensors and switches [23]. It is highly used in oxide electronic device applications because of its highly conductive nature. The electronic transport of LNO depends on the overlapping between Nickel (Ni) 3d and Oxygen 2p orbitals, which is very sensitive on the Ni-O-Ni bond angle. Other factors like doping, pressure, strain affect Ni-O-Ni bond angle and charge carriers density, which result a tuning in electronic behaviour [24]. From Fig 1.8 nickelates show the insulating behaviour as the size of rare earth ion decreases.

### **1.4.5-Motivation:**

The phase diagram of RNiO<sub>3</sub> gives us the opportunity to study the physical properties of oxide system by varying the parameters such as doping, strain, oxygen vacancy *etc.* In this family, LaNiO<sub>3</sub> remains in metallic state throughout the temperature range. Doping acts as controlling parameter of electronic transport in strongly correlated oxides by altering the carrier

concentration. Carrier concentration can be changed either by doping of divalent Sr, trivalent Nd and tetravalent Th ion at trivalent La-sites [25,26] or by doping of Mn, Fe, Cu, Zn, Mo, Ti, and W at Ni sites [27-29]. For Titanium (Ti), most stable oxidation state is 4 + in oxide state. The doping of tetravalent Ti at trivalent Ni sites can change valence state of Ni. As  $Ti^{4+}$  has no electron in its 3d band, so by replacing  $Ni^{3+}$  with less electronically active  $Ti^{4+}$  ion, we can drive the system towards the insulating state. Also, to maintain the charge neutrality of the compound, some of  $Ni^{3+}$  convert in  $Ni^{2+}$  that favours the insulating character of the system. To study the doping effect of Ti, we have synthesised  $LaNi_{1-x}Ti_x$  ( $x = 0-0.1$ ) thin films on  $LaAlO_3$  (LAO) single crystal substrate having thickness of 8nm.

## **Chapter 2-Experimental techniques**

This chapter introduces the synthesis method and characterization techniques used in this project work. The synthesis method includes preparation of bulk pellets by solid-state reaction method and thin films by pulsed laser deposition (PLD) method. For characterization, we have performed the X-ray diffraction method and Raman spectroscopy to analysis the structural behaviour. To study the electronic transport behaviour, we have performed temperature dependent resistivity measurement.

### **2.1- Sample preparation:**

It involves two process:

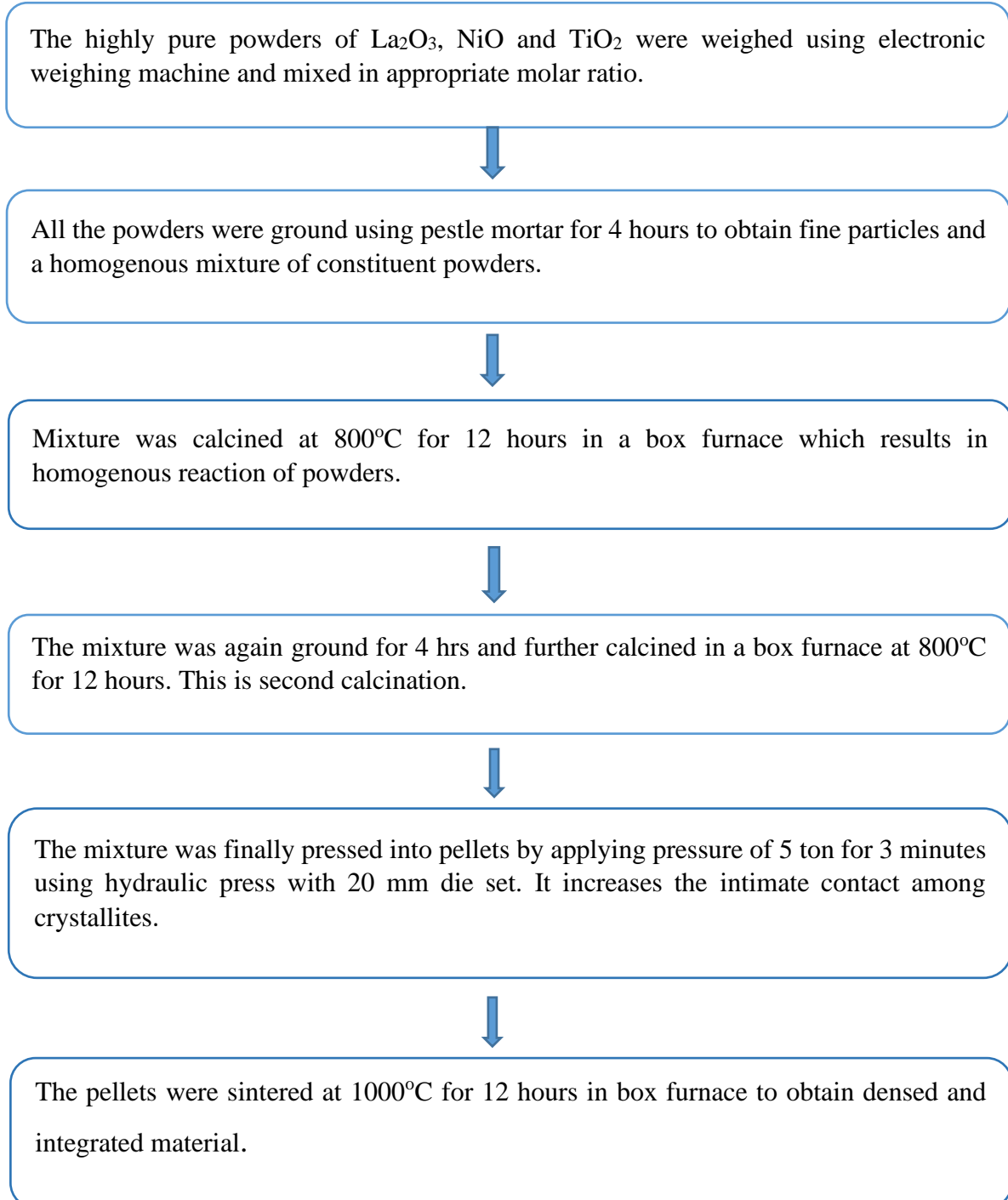
1. Bulk target synthesis (by solid-state reaction method).
2. Thin films synthesis (by Pulsed laser deposition method (PLD))

#### **2.1.1-Bulk target synthesis:**

Five bulk pellets of  $\text{LaNi}_{1-x}\text{Ti}_x\text{O}_3$  (LNTO) ( $x= 0, 0.01, 0.02, 0.05, 0.10$ ) each of weight 2.5g were prepared using solid-state reaction method. These pellets were used as targets for thin films deposition in PLD.

Solid-state reaction method is a solvent free method and is the most common technique used to synthesis bulk oxides [30]. Reactants in powder form are mixed homogeneously according to their molar proportion and are allowed to react. First, the highly pure powders are weighed and mixed in proper stoichiometric ratio. Mixture is ground to ensure that mixture is homogenously mixed. Grinding of powders decrease the particle size and increase the surface area of contact resulting in high reaction rate. Grinding is done using the pestle-mortar for 3-4 hours. In order to initialize the reaction, powder is heated at very high temperature because powders do not react at room temperature. This is known as calcination. During this process some impurities are removed. After this heating, second grinding is done for about 3-4 hours to maintain particle size. After this, powders are again calcinated to obtain single phase. Then, powders are pressed into pellets using hydraulic press with 20 mm die set. These pellets are heated in a temperature higher than calcination temperature to obtain the densified compound. This process is known as sintering.

We have prepared  $\text{LaNi}_{1-x}\text{Ti}_x\text{O}_3$  (LNTO) ( $x=0, 0.01, 0.02, 0.05, 0.10$ ) bulk targets using  $\text{La}_2\text{O}_3$ , NiO and  $\text{TiO}_2$  powders in proper stoichiometric ratio. The process of bulk synthesis is given in the block diagram.



### **2.1.2-Thin films synthesis using PLD:**

In modern era, thin films are widely used in making different devices (e.g. electronic devices, optical coating, instrument hard coatings *etc*). There are different techniques for thin film fabrication. We have deposited thin films using pulsed laser deposition (PLD) method on single crystal substrate LAO ( $\text{LaAlO}_3$ ) having (001) orientation. Lattice parameter of LAO and  $\text{LaNiO}_3$  is  $3.789 \text{ \AA}$  and  $3.837 \text{ \AA}$  respectively which causes strain in the films due to lattice mismatch.

### **Pulsed laser deposition method:**

This method is one of the most efficient method to synthesis thin films. The PLD instrument consists of a laser source (in this project, KrF Eximer laser of wavelength  $248 \text{ nm}$  is used) and a vacuum chamber which have substrate holder, target holder, heating element and process gas inlet. Mechanism of PLD is divided into two parts:

- A. Laser Interaction with material
- B. Thin film growth on substrate

#### **A- Laser interaction with material:**

A pulsed beam from laser is focused by focusing lens on the target material that should be deposited on the substrate. This interaction takes place in vacuum chamber where the vacuum and process gas pressure like Oxygen, Argon can be controlled. When the laser pulse of sufficient energy falls on the target, it ablates the material due to fast heating at the target [31]. Laser-target interaction and ablation of material is fast process. Within 30 ns, electromagnetic radiation absorption, melting of surface, vaporization and plasma formation takes place. The plasma plume consisting of ions, molecules *etc* is highly directed towards the substrate on which the film has to be deposited. Energy range of plasma plume is from  $0.1 \text{ eV}$  to  $10 \text{ eV}$  [32]. The shape of plasma plume depends upon the partial pressure of process gas. Kinetic energy and the scattering of the particles in the plasma plume also depend on the partial pressure.

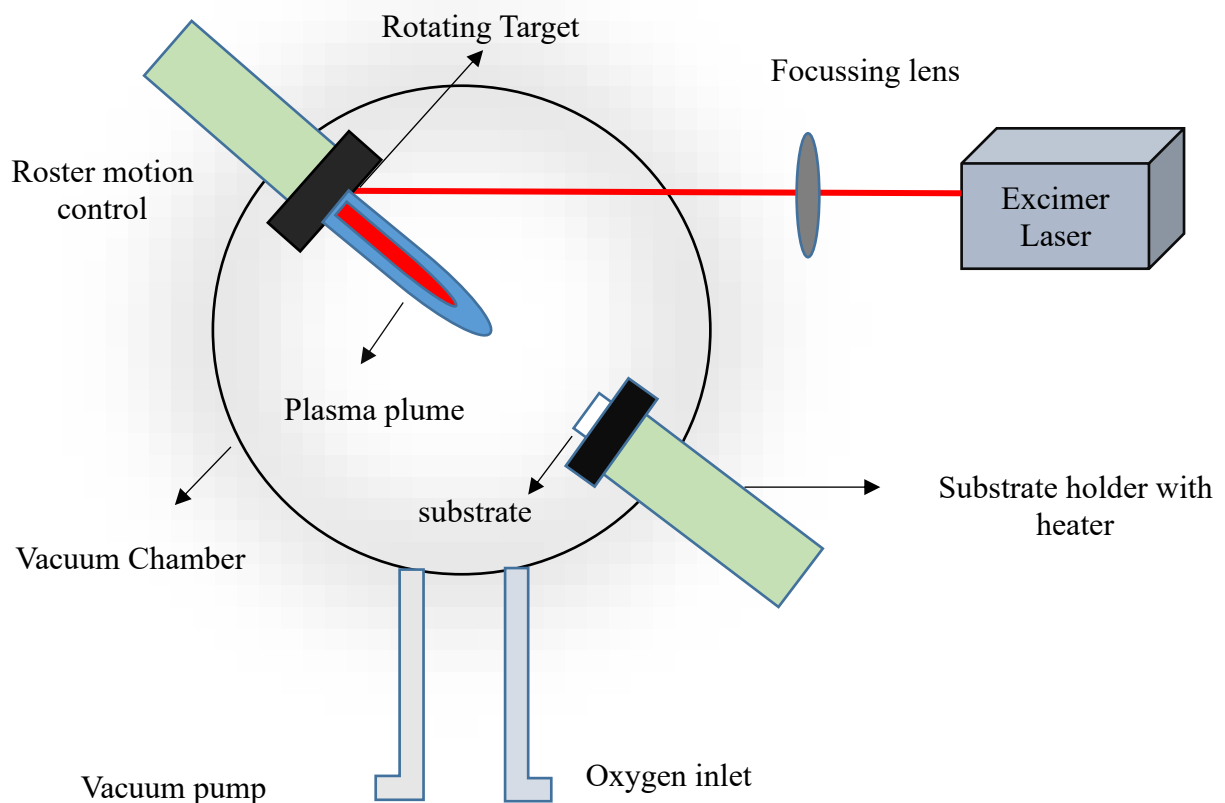


*Fig 2.1- Schematic of Pulsed laser Deposition Set-up*

**B-Thin film growth on substrate:**

There are three main growth technique

- a) *Island growth* – In this model, the film is grown in the three-dimensional islands form in which atoms or molecules of thin films are more strongly bound to each other than to the substrate.
- b) *Layer by layer growth*- It is two-dimensional growth mode and atoms or molecules get deposited in monolayer form on the substrate. In this mode, the growth of atoms or molecules of the thin films are strongly bound to the substrate as compared to each other.

c) *Mixed growth*- In this model, mixture of two-dimensional and three- dimensional growth of thin films take place. Up-to a few monolayers the layer by layer growth take place then it is followed by the island growth of thin film.

Some external parameters play crucial role in the phase stabilization, epitaxial nature and the quality of the thin films [32,33]. These parameters are

- i) *Laser energy*
- ii) *Partial pressure of process gas*
- iii) *Substrate temperature*
- iv) *Distance between substrate and target.*

Laser energy controls the kinetic energy of the particles and the growth rate. Process gas controls the plume shape and helps in stoichiometry of the complex oxides. Substrate temperature is important for the nucleation and growth process of thin film. Target to substrate distance determines the angular spread of the plasma plume.

Table 1 shows the parameters that are maintained during the deposition:

### **Advantage of PLD:**

- PLD provides flexibility to the deposition parameters such as laser energy, pressure of processing gas, substrate temperature, *etc.*
- Phase purity is maintained even for the multiphase target.
- Complete stoichiometry transfer from the target to substrate.
- Thickness of the thin film can be controlled.
- Multilayer films can be synthesised.

Unstable oxidation state can be stabilized which require high temperature and pressure.

<b>PARAMETERS</b>	<b>VALUES</b>
Laser energy	310 mJ
Base pressure of vacuum chamber	$\sim 5.0 \times 10^{-4}$ Pa
Target to Substrate distance	4.5 cm
Deposition temperature	720° C
Repetition rate	4 Hz
No. of Pulses	560
Oxygen Partial Pressure	40 Pa
Thickness of film	8 nm
Annealing gas, pressure	Oxygen, 1000 Pa
Annealing time	3 minutes

*Table 1- Parameters of PLD at the time of deposition*

## **2.2-Characterization techniques:**

Structural and electronic property are studied using characterization techniques. Structural characterization was studied using the X-Ray Diffraction and Raman Spectroscopy while electronic property was studied using temperature dependent resistivity measurement.

We have performed these techniques:

1. X-Ray Diffraction
2. Temperature dependent resistivity measurement
3. Raman spectroscopy

### **2.2.1-X-Ray Diffraction (XRD):**

This technique was discovered by Max Von Laue, W. L. Bragg and W. H. Bragg in 1912. It is the most common technique used to study the structural characterization for both crystalline and non-crystalline materials. Wavelength of the X-ray is of the order of  $\text{\AA}$  which is comparable to interatomic distance, hence it is a suitable tool to probe the structure of material. Using XRD, we get the information of lattice parameters, size of crystallite, chemical composition, strain etc [34].

XRD works on the principle of Bragg's law. In the cathode tube, filament is heated using alternating voltage applied between two electrodes. Free electrons of high velocity from filament travel from cathode to anode and strike at the anode surface that create the X-rays in tube. These X-rays are allowed to fall on the surface of sample and diffracted by the different atomic planes in the crystal structure. If this condition is satisfied, constructive interference occur between the diffracted beam and a peak of intensity will be observed with respect to  $\theta$ .

The Bragg' condition is given by:

$$2d\sin\theta = n\lambda$$

Here,  $d$  is inter-planer distance,  $\theta$  is angle of incidence,  $\lambda$  is wavelength of X-ray and  $n$  is order of diffraction.

For every material XRD pattern is unique, and thus can be considered as a signature of that material. This uniqueness helps to validate the purity of phase of that material. Thus, XRD pattern helps in providing information of lattice parameters, bond angles, grain size *etc*. Fig 2.2 shows the schematic diagram of the XRD. Here,  $\Omega$  is angle between X-ray beam and sample surface,  $2\theta$  is angle

between the incident and diffracted beam,  $\phi$  is angle of rotation about the plane

perpendicular to sample surface and  $\Psi$  is angle about the line parallel to the sample surface.

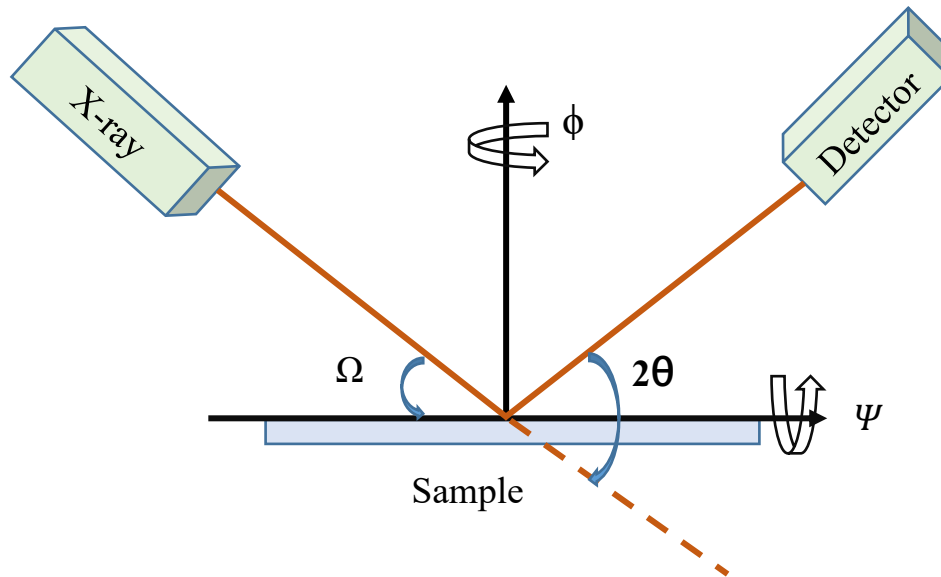


**Fig 2.2- Schematic of X-Ray Diffraction set-up**

Due to lattice mismatch between the thin film and the substrate, thin film tries to attain the lattice parameter of the substrate which results strain in the thin film. There are two types of strain:

1. *Tensile Strain*
2. *Compressive Strain*

In tensile strain, the lattice parameter of the substrate is greater than that of the thin films as shown in Fig 2.3, So the film tries to stretch itself, which results in shrinking of out-of-plane lattice parameter and XRD pattern shift towards right in accordance to the Bragg's law.

In compressive strain, the lattice parameter of the substrate is smaller than that of the thin films as shown in Fig 2.4, So the film tries to compress itself, which results in expansion of out-of-plane lattice parameter and XRD pattern shift towards left in accordance to the Bragg's law.

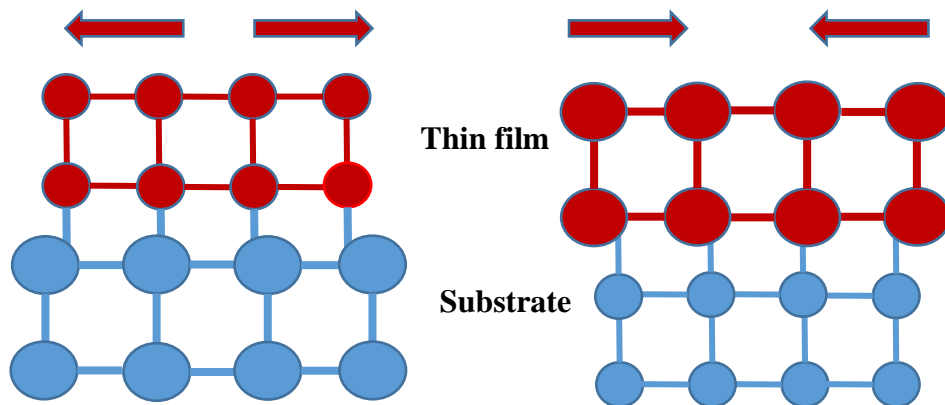


**Fig 2.3- Film showing Tensile strain**

**Fig 2.3- Film showing Compressive strain**

### **2.2.2-Temperature dependent resistivity measurement:**

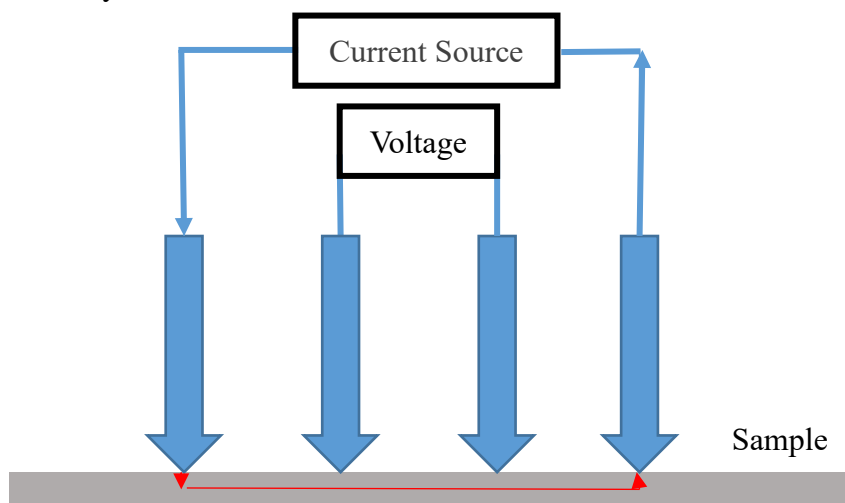
It provides information about the resistance to flow of charge produced by the lattice under the application of the Electric Field. Depending upon the value of resistivity, materials are classified as metals, semiconductors or insulators. Resistivity of the materials vary with the temperature. In metals, resistivity increases with increase in temperature, while in insulators it decreases with increase in temperature. Resistivity can be measured by two probe method or four probe method. The advantage of four probe method is that it eliminates the contact resistance by using separate probes for source and measurement. This is very useful to find the resistance of the sample that has very low resistance.

Fig 2.5 shows the four-probe set up. It is the most widely used instrument to measure electrical resistivity. In this method, the potential drop across two probes is measured and distance between these two probes is considered as sample length [36]. Formula for resistivity of the samples is given by:

$$\rho = \frac{VA}{DI}$$

Where A is Area of sample, D is distance between the probes, I is current and V is potential difference between two probes.

This method can determine resistivity of thin film as well as of the single crystal. Outer contacts of sample are used for the current flow and potential difference produced by that current is measured through inner contacts of the sample. As the effects of contact resistance are eliminated in this method, so it is most suitable method to measure to calculate small resistance accurately [37].



***Fig 2.5- Four probe set-up***

S

The temperature dependent resistivity measurements have been performed in Closed Cycle Refrigerator (CCR) Cryostat using four probe method in the temperature range of 300K-12K. Silver paste of Epoxy technology (EPO-TEK EE 129-4) was used to make the ohmic contact between metallic wire and sample surface. As in  $\text{RNiO}_3$  compounds, thermal hysteresis in temperature dependent resistivity is observed which is a manifestation of first order metal to insulator transition. Resistivity of thin films was recorded with heating and cooling of the sample with a constant rate of 4K/min.

Resistivity measurement was performed in a JANIS RESEARCH CCR cryostat. Keithely 2612A was used as source meter as well as voltage meter. Liquid He was used in CCR cryostat. After attaining the good vacuum, measurement was performed with the help of LABVIEW RT-5d in a temperature range of 300K-12K.

### **2.2.3-Raman Spectroscopy:**

This method was invented by Indian physicist C.V. Raman for which he was awarded nobel prize in 1930. It can be used for both qualitative analysis and quantitative analysis of the samples. The frequency of scattered radiations is used for qualitative analysis while intensity of scattered radiations is used for quantitative analysis.

This technique is based on the Raman Effect [38]. According to Raman Effect, when monochromatic radiation incident on the samples, frequency of small fraction of scattering radiation different of the incident radiation. Raman Scattering is the inelastic scattering between the radiation and the molecules of the sample. It is used to probe the molecular vibration.

In Raman Spectroscopy, a monochromatic beam of laser is incident on the sample which interacts with the molecules present in the sample. The scattered light has a frequency different from the incident radiation. This scattered light is used to construct Raman Spectrum. When monochromatic radiation incidents on sample, after interaction with molecules of sample, scatters in all directions. Most of the scattered radiation has the same frequency as that of the incident radiation. This scattering is known as Rayleigh scattering. Some part of the scattered radiation has frequency different from that of incident radiation and this scattering is called Raman scattering [39]. If the frequency of scattered radiation is lower than the frequency of the incident radiation, the lines observed in Raman spectrum is known as Stokes lines and if

the frequency of scattered radiation is higher than the frequency of the incident radiation, the lines observe in Raman spectrum is known as Anti-Stokes lines [40] as shown in Fig 2.6.

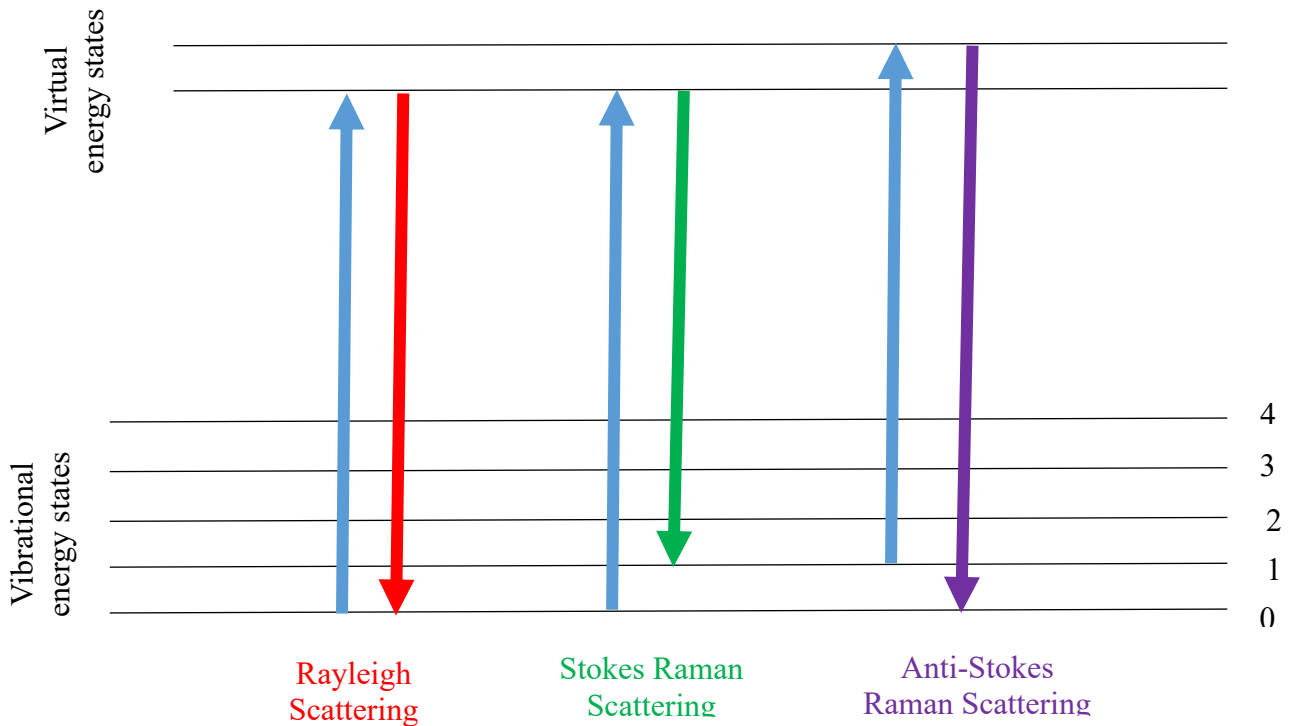


**Fig 2.6- Schematic representation of Rayleigh and Raman Scattering.**

In Stokes shifted Raman bands, the vibrational energy levels goes from lower to higher, thus Stokes bands are more intense than Anti-Stokes bands. This is why, in conventional Raman spectroscopy Stokes bands are observed.

A conventional Raman Spectrometer consists the following components:

- i) *A laser source*
- ii) *Lens to focus the light on the sample*
- iii) *A Monochromator unit*
- iv) *A single processing system consisting a detector and a data processing unit*

The schematic diagram of the Raman spectrometer is shown in Fig 2.7.

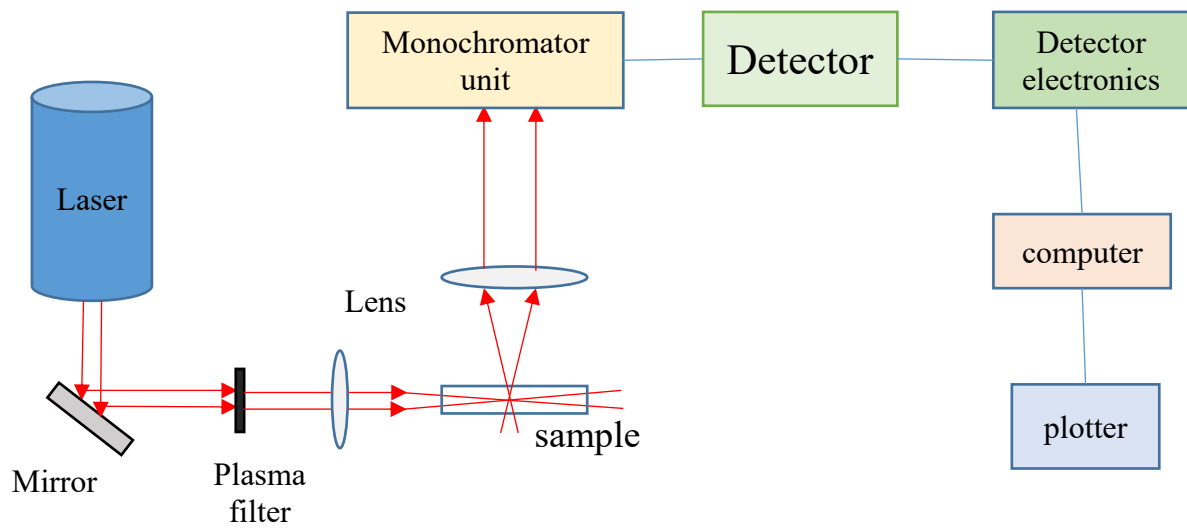


***Fig 2.7- Schematic diagram of Raman spectroscope***

Vibrational modes analysis of thin films was done using LABRAM micro-Raman spectrometer with 632.8 nm wavelength of the laser. At room temperature,  $\times 100$  lens was used to collect Raman scattered signals while  $\times 50$  lens was used to collect Raman scattered signals in temperature dependent Raman spectroscopy. Liquid N<sub>2</sub> was used as coolant and temperature range of measurement was 93-300 K.

## CHAPTER 3 - RESULTS AND DISCUSSION

We have prepared five samples of Ti-doped  $\text{LaNiO}_3$  thin films on the single crystal substrate  $\text{LaAlO}_3$  (LAO) using pulsed laser deposition method. Ti was doped at Ni site and the percentage of doping was 0%, 1%, 2%, 5% and 10%. The thickness of all the films was 8 nm. We have performed XRD and Raman Spectroscopy for structural analysis and temperature dependent resistivity measurements to study electronic behaviour.

### 3.1-X-Ray Diffraction:

X-ray diffraction (XRD) is an elastic-scattering *i.e.* energy of the X-ray does not change after scattering. It gives us information about the crystal structure, grain size, chemical composition *etc.* of both bulk materials and thin films. We have done XRD measurement using PanAnalytical made set up to examine the phase purity and epitaxial strain in  $\text{LaNi}_{1-x}\text{Ti}_x\text{O}_3$  ( $x=0-0.10$ ) (LNTO) thin films.

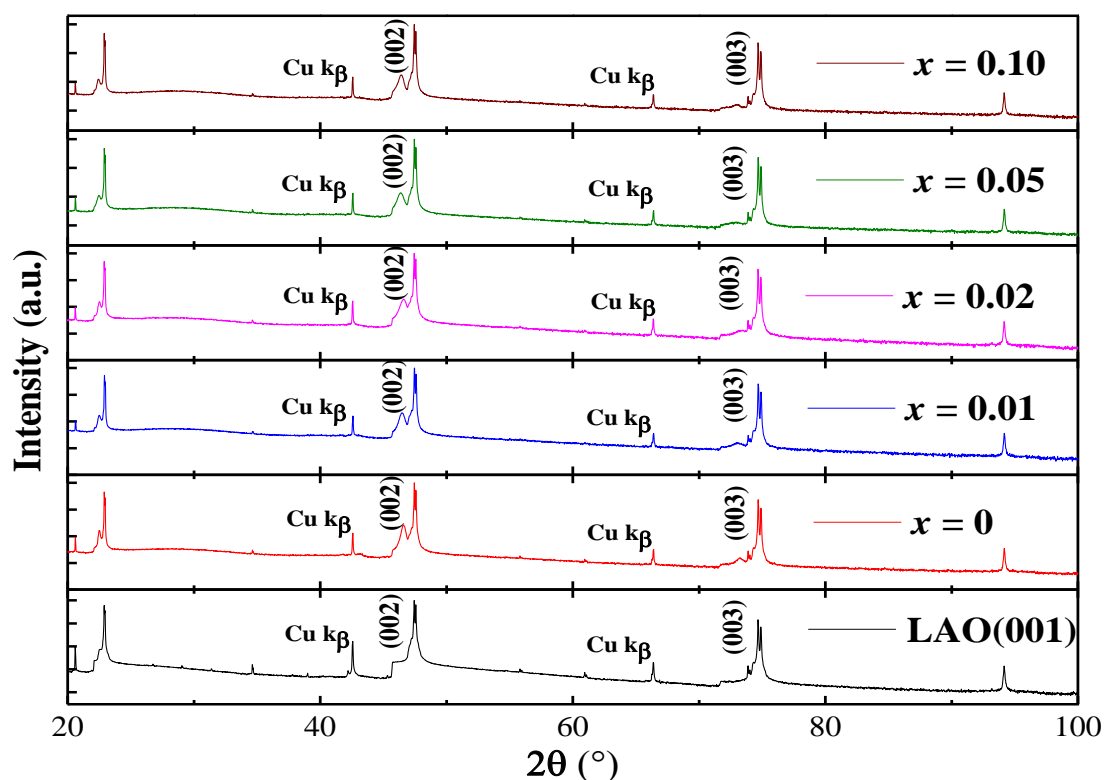


*Fig 3.1- X-ray diffraction of  $\text{LaNi}_{1-x}\text{Ti}_x\text{O}_3$  ( $x=0-0.10$ ) thin films grown on LAO (001) substrate.*

Fig 3.1 shows XRD pattern of LNTO thin films on LAO substrate. From this pattern, we found that all the thin films are pure and grown in the same direction of LAO (001) crystallographic axis. As the pseudo-cubic lattice parameter of  $\text{LaNiO}_3$  is  $3.837\text{\AA}$  and that of LAO is  $3.789\text{\AA}$ , the lattice mismatch is approximately  $-1.26\%$ . When the thin film of  $\text{LaNiO}_3$  is deposited on LAO, because of the lattice mismatch between substrate and thin film, the thin film's unit cell contracts. The in-plane lattice parameter of thin film decreases and to keep the volume of the unit cell constant, the out-of-plane lattice parameter increases. So according to Bragg's law

$$2d\sin\theta=n\lambda$$

Where,  $d$  is the interatomic planer distance which is out-of-plane lattice parameter,  $n$  is the diffraction order,  $\theta$  is the angle of diffraction and  $\lambda$  is wavelength of X-ray.

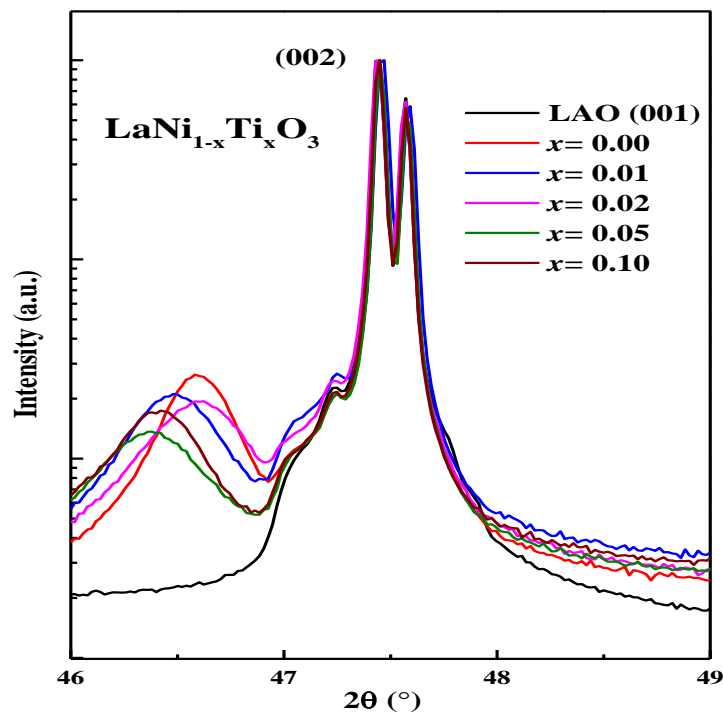


*Fig 3.2- Enlarge view of (002) Bragg diffraction of  $\text{LaNi}_{1-x}\text{Ti}_x\text{O}_3$  ( $x=0-0.10$ ) thin films.*

Keeping other parameters constant, the value of  $\theta$  decrease with increase in  $d$ . Thus, the peak of diffraction shifts towards the lower  $2\theta$  value. Fig 3.2 shows the enlarged view of (002) Bragg's diffraction plane. As we can see that there is systematic shift of peak towards the left side as we increase doping. This shifting is known as compressive strain. The substrate peak of all the thin films lies along the same position and peak of all the thin films lies towards the left of substrate peak as shown in Fig 3.2. With Ti doping, there is no systematic shifting of the peaks of thin films and all peaks mostly lie around the same position.

### 3.2-Temperature dependent resistivity measurement:

In order to know about the electrical behaviour of the thin films, we have performed temperature dependent resistivity measurements. Four probe resistivity setup in JANIS made Close Cycle Refrigerator cryostat was used to measure the temperature dependent resistivity of thin films.

Fig 3.3 shows the plots of resistivity vs temperature for all the films of  $\text{LaNi}_{1-x}\text{Ti}_x\text{O}_3$  ( $x=0.0-0.10$ ). From these plots, we find that all the thin films remain metallic throughout the temperature range of 300K-12K. No film shows metal to insulator transition. The resistivity of thin films increases as the doping percentage of Ti increases. This means system is going towards the insulating state. As Ti has vacant d orbital, so it will not take part in conduction thus introduces the insulating behaviour to the system.

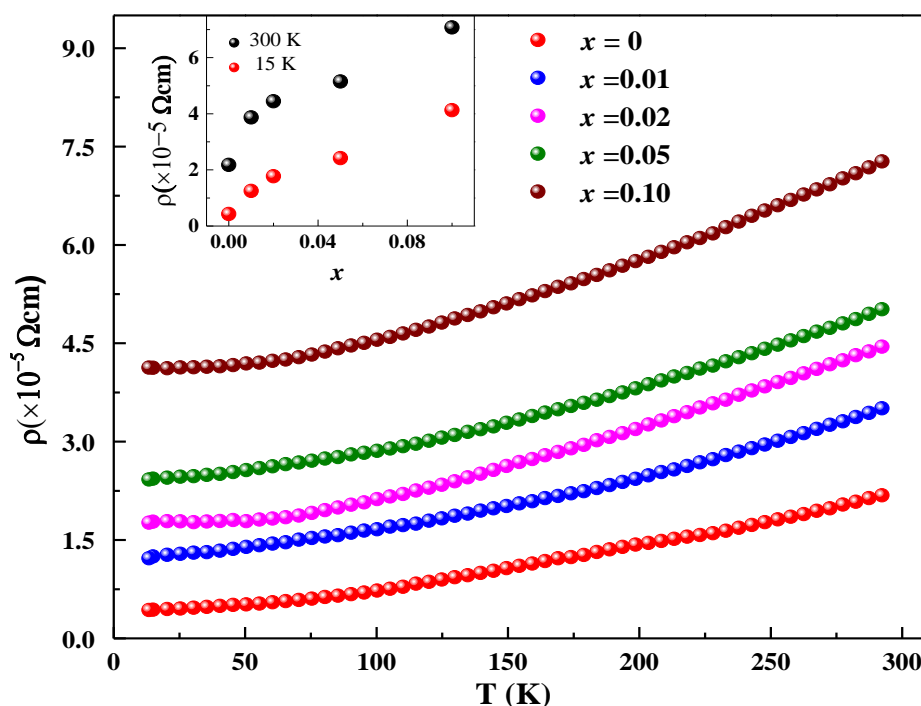


**Fig 3.3-** Resistivity vs temperature plots for  $\text{LaNi}_{1-x}\text{Ti}_x\text{O}_3$  ( $x=0.0-0.10$ ) thin films on LAO (001). The inset figure shows resistivity vs doping at room temperature (300 K) and 15 K.

As we know, according to Zaanen Sawatzky Allen model, RNiO<sub>3</sub> compounds lie in the charge transfer gap insulators category [6] where the coulombic interaction energy  $U$  is greater than the energy difference  $\Delta$  between vacant Ni  $3d$  orbital and oxygen  $2p$  orbital. In recent studies of RNiO<sub>3</sub>, it has been reported that charge transfer gap is very small (sometimes negative) [40]. That's why, ground state of these compounds is considered a mixture of  $3d^7 2p^6$  and  $3d^8 L$  configuration, where  $L$  is a legend hole in  $2p$  oxygen band [27]. It has been reported that the presence of Ni<sup>2+</sup> favours the insulating state by decreasing the band width. In LaNiO<sub>3</sub>, Ti acquire 4+ oxidation state. To maintain the charge neutrality, some Ni<sup>3+</sup> convert in Ni<sup>2+</sup> and thus decrease the band width *i.e.* increase the charge transfer gap alongwith decrease in charge density in  $d$  band [41]. This decreases the orbitals overlapping which result increase in the resistivity of the system.

We have fitted power law equation on temperature dependent resistivity plots. The power law is given by

$$\rho_{\text{NFL}} = \rho_0 + AT^n$$

where,  $\rho_0$  is residual resistivity,  $A$  is constant that denotes the strength of electron-electron scattering [42]. For  $n=2$ , system is considered as Landau Fermi Liquid (LFL). However,  $n < 2$  is also observed which is deviation to Non-Fermi Liquid (NFL) [43,44]. In our system  $n=1.3$  and  $n= 1.6$  are observed which indicate that system lies in semi-classical region. Fig 3.4 shows the resistivity vs temperature plot fitted according to power law equation.

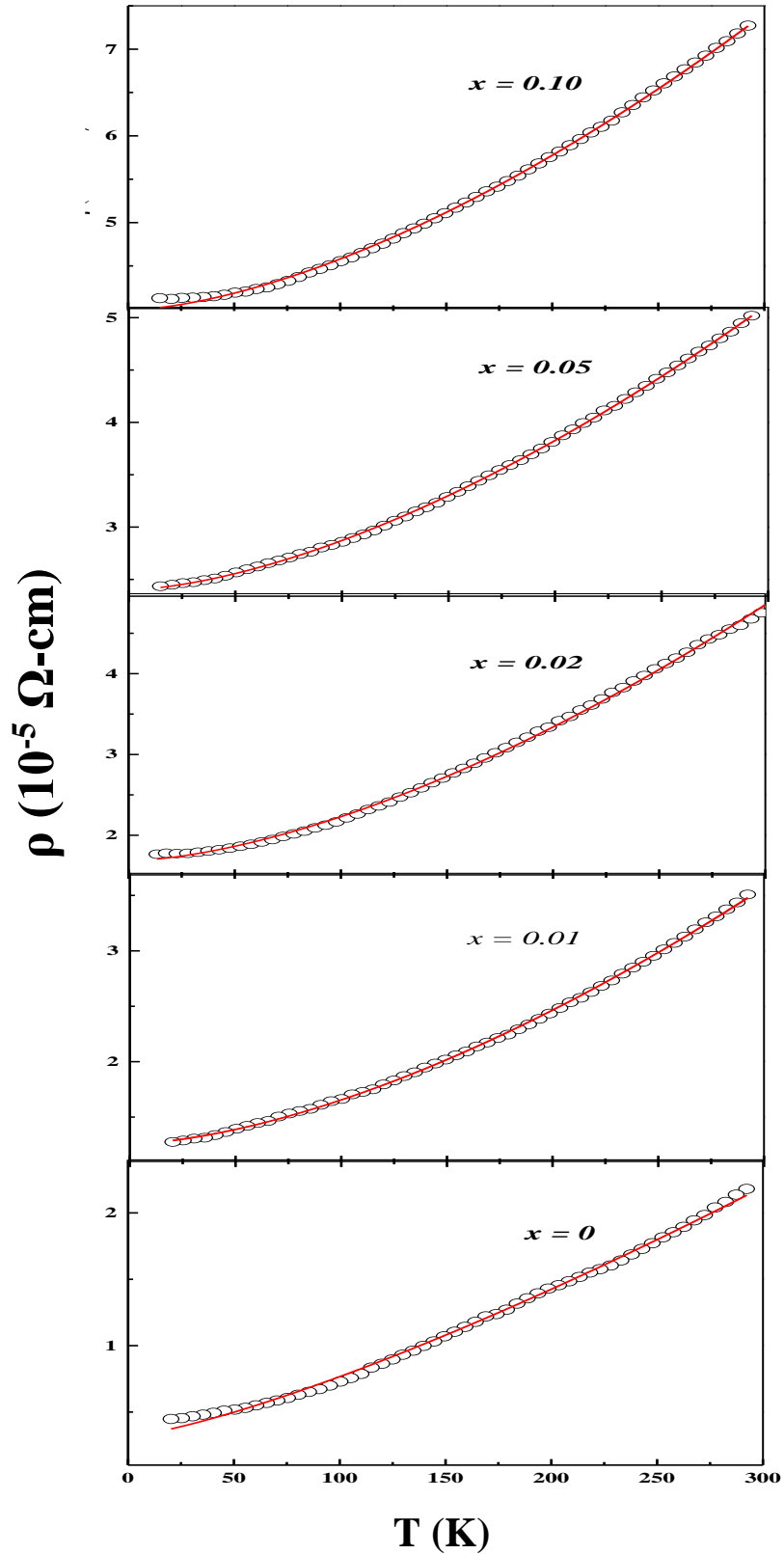


*Fig 3.4- Resistivity vs temperature plots for  $\text{LaNi}_{1-x}\text{Ti}_x\text{O}_3$  ( $x=0.0-0.10$ ) thin films on LAO (001). The red line shows fitting of resistivity using power law equation*

Fitting parameters are shown in table-1. The parameter  $n$  is adjustable and  $n= 1.6$  and  $n= 1.3$  are obtained from the fittings of power law equation indicating Non-Fermi Liquid (NFL) behaviour. For pure film,  $n= 1.3$  NFL behaviour is observed and for Ti-doped films  $n= 1.6$ . Residual resistivity  $\rho_0$  increases with increasing Ti-doping as shown in table-2.

$x$	$N$	$A (\times 10^{-9})$ $(\Omega\text{-cm}(\text{K}^n)^{-1})$	$\rho_0 (\times 10^{-5})$ $(\Omega\text{-cm})$
0	1.3	$11.321 \pm 0.078$	$0.316 \pm 0.007$
0.01	1.6	$2.519 \pm 0.007$	$1.256 \pm 0.003$
0.02	1.6	$3.449 \pm 0.015$	$1.683 \pm 0.007$
0.05	1.6	$2.968 \pm 0.005$	$2.401 \pm 0.002$
0.10	1.6	$3.715 \pm 0.014$	$3.991 \pm 0.006$

*Table.2- Transport properties of  $\text{LaNi}_{1-x}\text{Ti}_x\text{O}_3$  ( $x= 0-0.10$ ) thin films deposited on LAO.*

### **3.2.3-Raman Spectroscopy:**

It is the inelastic scattering of the light in a substance where incident light transfers some energy to molecular vibrations. The spectrum of the scattered light represents a chemical fingerprint of the substance.

The Raman Spectroscopy was used to study vibrational modes of the thin films. The group theory gives five Raman active modes ( $A_{1g}$  and four  $E_g$ ) for LNO [47,48]. In our measurement, we observe two modes  $A_{1g}$  and  $E_g$ . The  $A_{1g}$  mode describes the rotations of  $NiO_6$  about the trigonal axis [111] that is directly related to the octahedral tilt angle and the  $E_g$  modes describes bending of Ni-O bond [47]. Earlier, it has been reported that  $A_{1g}$  mode and  $E_g$  mode for thin film of LNO on single crystal LAO observed at  $214\text{ cm}^{-1}$  and  $403\text{ cm}^{-1}$  respectively [45]. In the present study,  $A_{1g}$  and  $E_g$  (bending of Ni-O bond) modes for parent LNO are observed nearly at  $196\text{ cm}^{-1}$  and  $402.5\text{ cm}^{-1}$  respectively as shown in Fig 3.5.

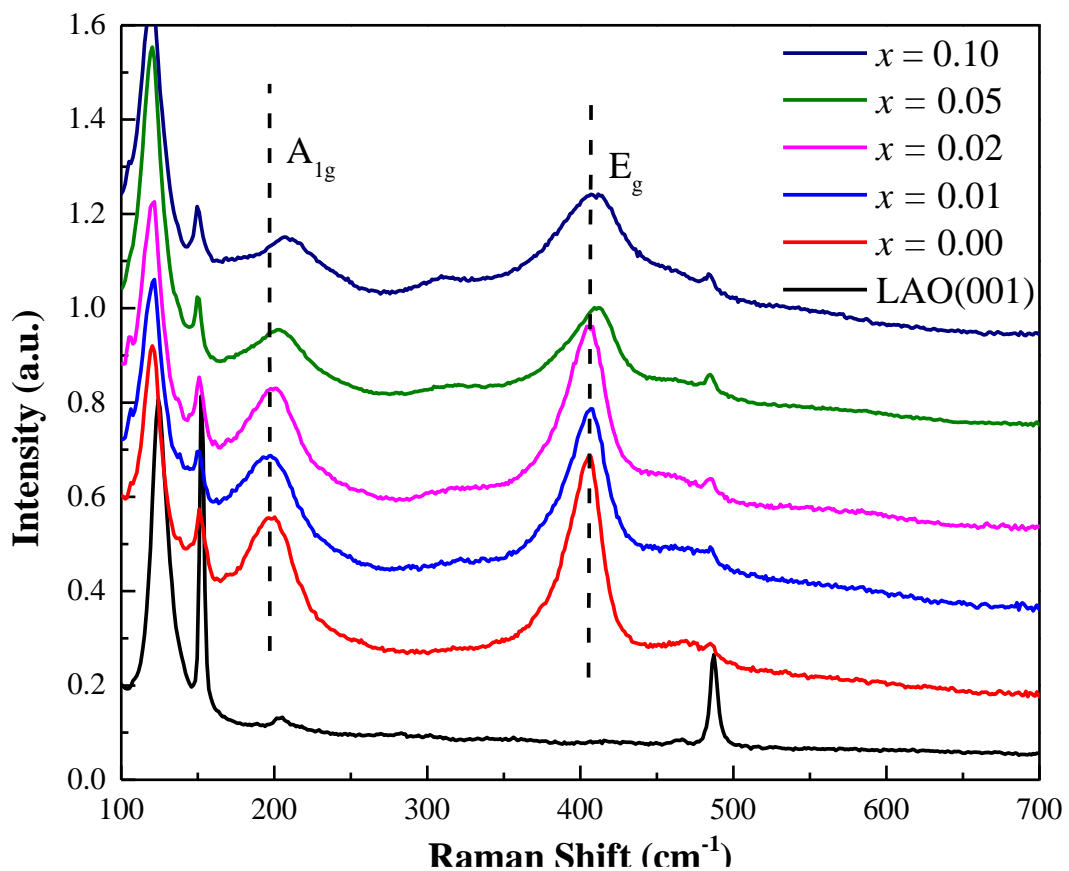


**Fig 3.5- Room temperature Raman Spectra of  $LaNi_{1-x}Ti_xO_3$  ( $x=0.0-0.10$ ) thin films.**

Broadening of the modes is related to FWHM (full width at half maximum). It was observed that there is broadening of  $A_{1g}$  and  $E_g$  modes with the increase of doping of Ti in the system. This broadening is more pronounced for  $A_{1g}$  mode. It is also observed that by increasing the doping percentage of Ti, both the  $A_{1g}$  and  $E_g$  modes are blue-shifted but in case of  $E_g$  mode the Raman shift is not systematic as shown in Fig 3.6. Earlier reports suggested that the shifting of  $A_{1g}$  mode is  $-23\text{ cm}^{-1}$  per degree shift in  $NiO_6$  octahedral angle [46-49]. So, by

increasing the doping of Ti from undopedS to 10%, the shift in  $A_{1g}$  mode is nearly  $13 \text{ cm}^{-1}$ . If this shift is converted into the tilt in Ni-O-Ni octahedral angle, then it is nearly equals to  $0.56^\circ$  with respect to undoped film. Plotting parameters of Fig 3.6 is in table 2.

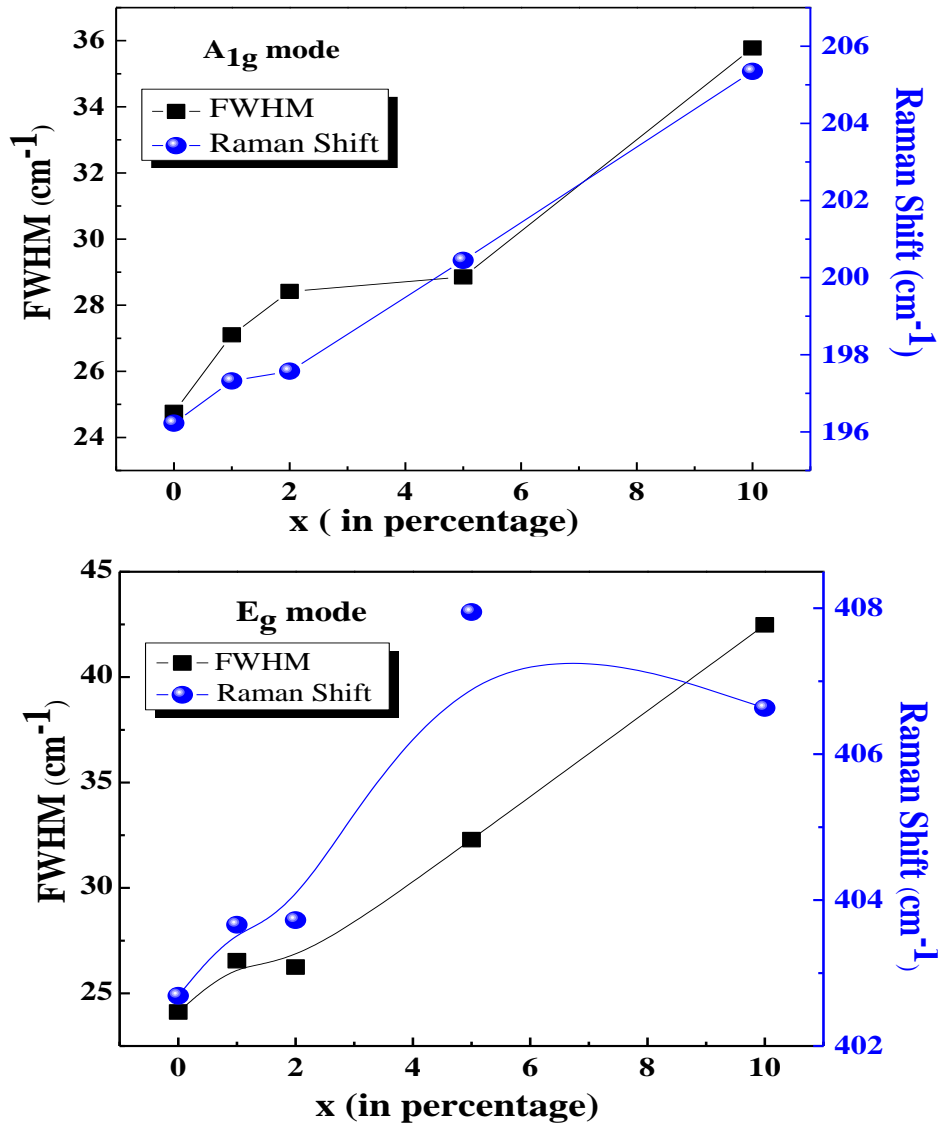
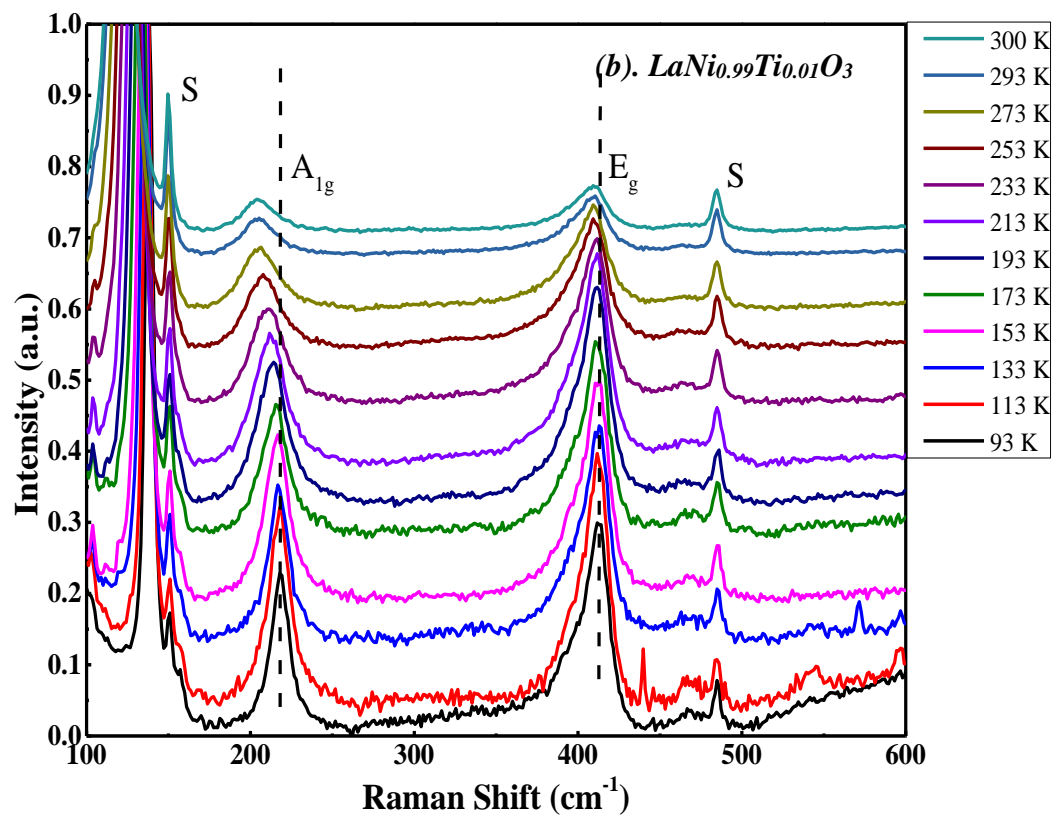
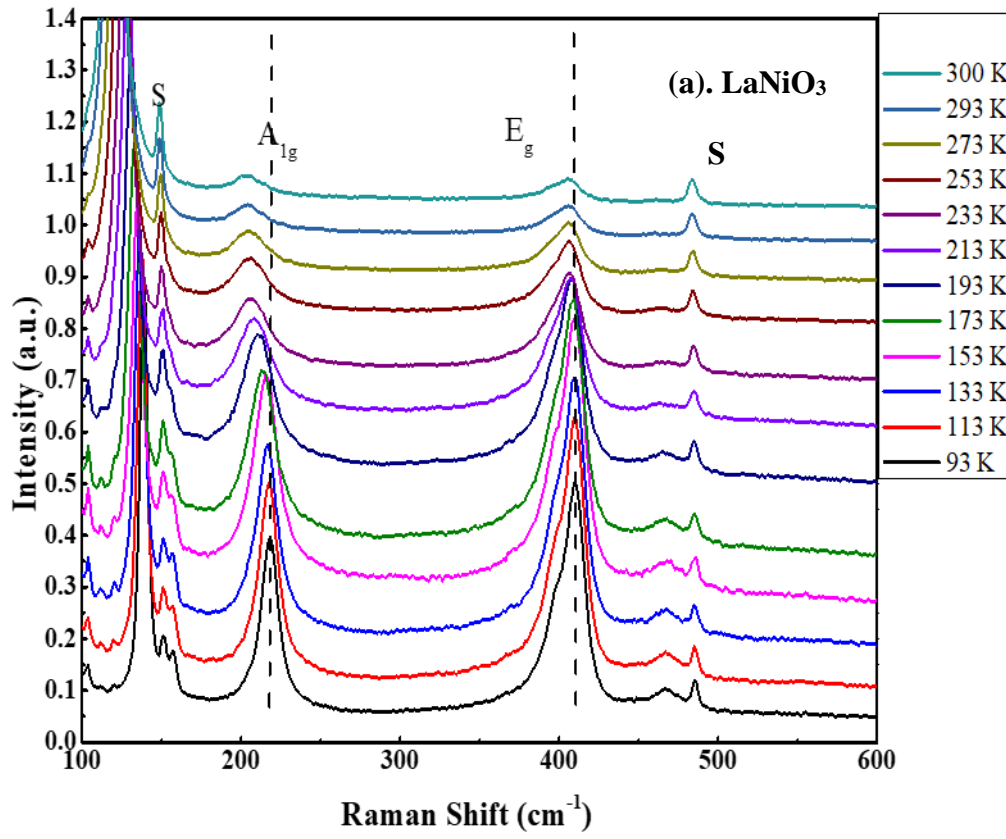


**Fig 3.6- Percentage Doping of Ti vs FWHM and Raman Shift of  $LaNi_{1-x}Ti_xO_3$  ( $x=0.0-0.10$ ) thin films.**

X (in percentage)	A <sub>1g</sub> mode		E <sub>g</sub> mode	
	FWHM (cm <sup>-1</sup> )	Raman Shift (cm <sup>-1</sup> )	FWHM (cm <sup>-1</sup> )	Raman Shift (cm <sup>-1</sup> )
0	24.7589 ± 1.2975	196.2280 ± 0.2830	24.1082 ± 1.1059	402.6877 ± 0.2955
1	27.1007 ± 1.4360	197.5755 ± 0.2913	26.5420 ± 0.8861	403.6615 ± 0.2150
2	28.4153 ± 1.5828	197.3214 ± 0.3335	26.2428 ± 0.8309	403.7258 ± 0.2119
5	28.8527 ± 1.6428	200.4478 ± 0.3818	32.2912 ± 1.1943	407.9472 ± 0.2911
10	35.7803 ± 1.8469	205.3487 ± 0.4066	42.4833 ± 0.8729	406.6238 ± 0.1675

**Table.3- - Fitting parameters of FWHM and Raman Shift shown in Fig-3.6.**

To study the effects of temperature variations on the Raman modes, we performed the Raman measurements in the temperature range of 93-300K for all the samples. The lack of appearance and disappearance of any Raman mode indicates a stable structure throughout the measured temperature range. Both the Raman mode A<sub>1g</sub> and E<sub>g</sub> are affected by the change in temperature, although neither disappears as shown in Fig 3.7. The A<sub>1g</sub> mode is red-shifted in all the systems with increase in temperature. Such a shift indicates the temperature influence on the rotation of NiO<sub>6</sub> octahedra. The E<sub>g</sub> mode is also showing red-shift (not as large as A<sub>1g</sub> mode) for all the films with increase in temperature and suggests the bending of Ni-O-Ni bond. There is significant change in FWHM A<sub>1g</sub> and E<sub>g</sub> mode observed with temperature. In all samples the FWHM increases with temperature increases as expected due to thermal broadening. But the overall spectrum is maintained in all the films and no drastic change occur, which suggests LaNiO<sub>3</sub> does not undergo phase transition in the investigated temperature range.



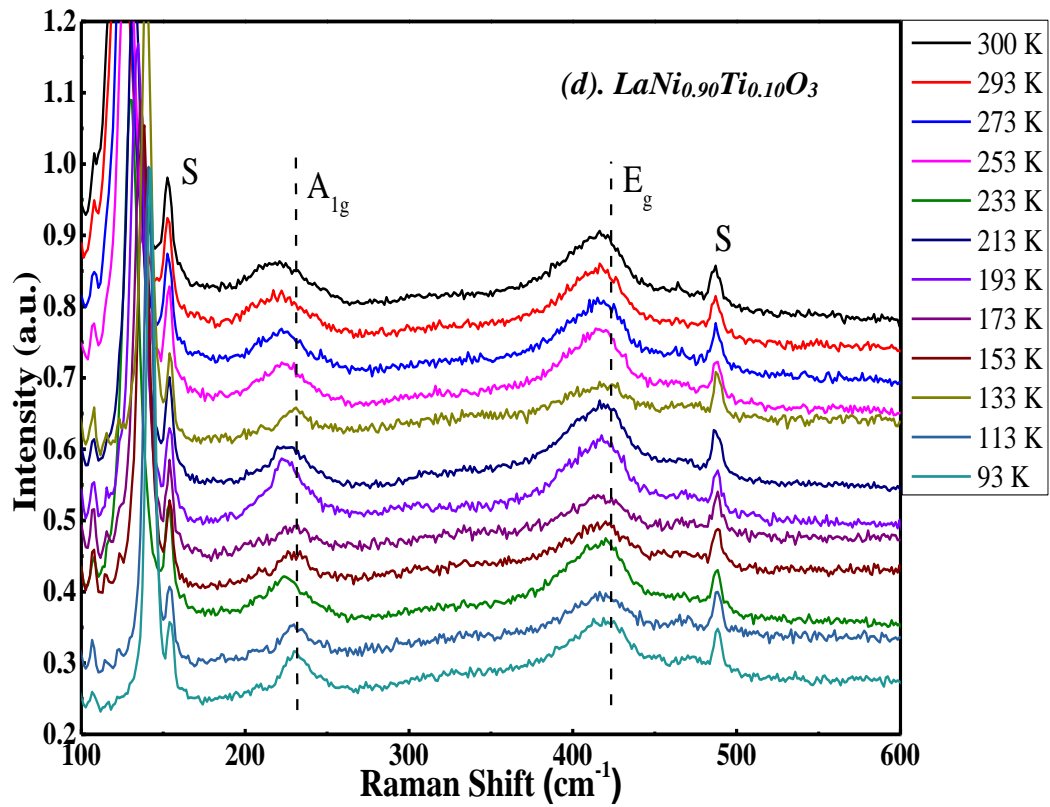
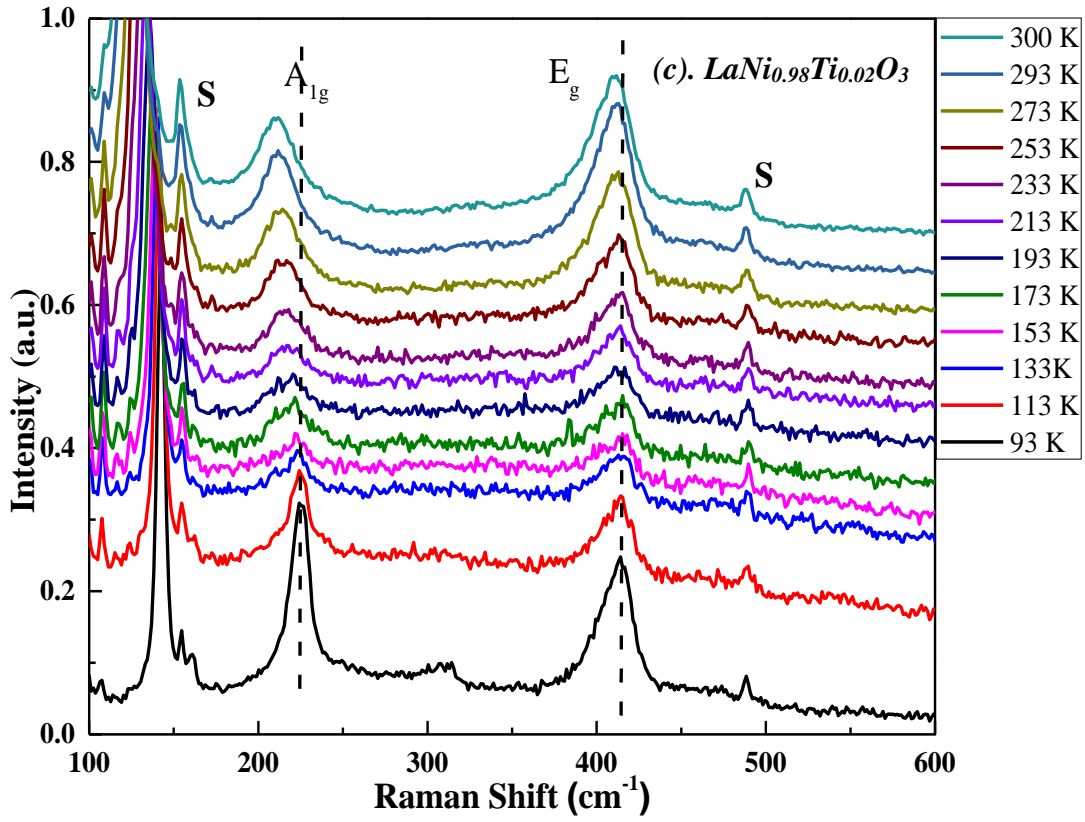


Fig 3.7- Temperature dependent Raman spectroscopy of  $LaNi_{1-x}Ti_xO_3$  ( $x=0.0-0.10$ ) thin films.

## **Conclusion:**

We have studied the effect on doping on the structural and the electronic properties of  $\text{LaNi}_{1-x}\text{Ti}_x\text{O}_3$  ( $x = 0-0.10$ ) thin films deposited on single-crystal LAO substrate. These changes in system are observed by increasing doping of Ti.

1. XRD peaks of the thin films shifted towards lower  $2\theta$  indicating the compressive strain experience by thin films.
2. Temperature dependent resistivity shows that all the films are metallic throughout the temperature range and the resistivity of the system increases with doping.
3. The theoretical fitting of resistivity suggested that in large temperature range system persisted non-Fermi liquid behaviour with  $n=1.3$  for undoped film and  $n=1.6$  for doped films.
4. The room temperature Raman spectroscopy shows that there is blue shift Raman spectra with doping.
5. Increase in bending and Rotation of Ni-O-Ni bonds with reduction in temperature has been seen in the temperature dependent Raman spectroscopy and the Raman spectra is red shifted.

## References:

1. James M. Rondinelli, Steven J. May, and John W. Freeland, *MRS Bulletin*, 2012, 37, 261.
2. Ramesh R, Complex functional oxide heterostructures, *Current Science*, 2013, 105,8.
3. Hill N.A., Why Are There So Few Magnetic Ferroelectrics?, *Journal of Physical Chemistry B*, 2000, 104, 6694-709.
4. Tejuca L.G., Fierro J.L.G, Properties and applications of Perovskite-Type Oxides, *CRC press*, 1992
5. Peña M. A., Fierro J.L.G., Chemical Structures and Performance of Perovskite Oxides, *Chemical Reviews*, 2001, 101, 1981-2018.
6. Medarde M.L., Structural, magnetic and electronic properties of RNiO<sub>3</sub> perovskites (R= Rare Earth), *Journal of Physics: Condense Matter*, 1997, 9, 1679.
7. Catalan G, Progress in perovskite nickelate research, *Phase Transition: a Multinational Journal*, 2008, 81, 729–749.
8. Khomoskii D.I., Transition metal compounds, *Cambridge University Press*, 2014, 1<sup>st</sup> edition.
9. Blundell S., Magnetism in Condensed Matter, *Oxford University Press*, 2001, 1<sup>st</sup> edition.
10. Torrance J. B., Lacorro P., Asavaroengchai C. and Metzger R.M., Simple and perovskite oxides of Transition-metals: Why some are metallic, while most are insulating, *Journal of Solid State Chemistry*, 1991, 90, 168-72.
11. Free Electron Model, Wikipedia 2018.
12. Garcia-Muñoz J.L., Rodriguez-Carvajal J., Lacorre P., and Torrance J.B., Neutron-diffraction study of RNiO<sub>3</sub> (R = La, Pr, Nd, Sm): Electronically induced structural changes across the metal-insulator transition, *Physical Review B*, 1992, 46, 4414-25.
13. Stoner I, Band Theory and Mott-Hubbard Insulators, *Physical Review B*, 1991, 44, 943.

14. Hubbard Model , 2018, *Wikipedia*.
15. Mott N. F., Metal-Insulator Transitions, Taylor and Francis, London , 1974.
16. Zaanen J., Sawatzky G. A., and Allen J.W., Band gaps and electronic structure of transition-metal compounds, *Physical Review Letter*, 1985, 55, 418-21.
17. Mikheev E., Hauser A.J., Himmertoglu B., Moreno N.E., Janotti A., Van de Walle C.G., and Stemmer S., Tuning Bad metal and non-metal Fermi liquid Behaviour in a Mott material: Rare earth nickelate thin films, *Science Advances*, 2015, 1, e1500797-e1500797.
18. Wang L., Chang L., Yin X., Rusydi A., You L., Zhou Y., Fang L., and Wang J., Localization-drive metal to insulator transition in epitaxial hole- doped  $\text{Nd}_{1-x}\text{Sr}_x\text{NiO}_3$  ultrathin films, *Journal of Physical: Condense Matter*, 2017, 29, 025002.
19. Yang Z., Ko C., Ramanathan P., Oxide electronics utilizing ultrafast metal to insulator transitions, *Annual Review Material Research*, 2011, 41, 337.
20. Catalano S., Gibert M., Fowlie J., Iniguez J., Triscone J.M., and Kreisel J., Rare-earth nickelates  $\text{RNiO}_3$ : thin films and hetrostructures, *Reports on Progress in Physics*, 2018, 81, 046501.
21. Fowlie J., Electronic and structural properties of  $\text{LaNiO}_3$ -based hetrostructures, *Springer International Publishing*, 2019.
22. Liu J., Kargarian M., Kareev, Gray B., Ryan P.J., Cruz A., Tahir Y., Chauang D., Guo J., Rondinelli J.M., Freeland J.W., Fiete G.A., Chakhalian J., Heterointerface engineered electronic and magnetic phases of  $\text{NdNiO}_3$  thin films., *Nature Communication*, 2013, 4, 2714.
23. Kyung Hwang D., Kim S., Lee J.H., Hwang L.S., Kim L.D., Phase evolution of perovskite  $\text{LaNiO}_3$  nanofibres for supercapacitor application and p-type gas sensing properties of  $\text{LaOCl-NiO}$  composite nanofibers, *Journal of Materials Chemistry*, 2011, 21,1959-65.
24. Catalan G., Bowman R.W., Gregg J.M., Metal-insulator transitions in  $\text{NdNiO}_3$  thin films, *Journal of Applied Physics*, 2000, 62, 7892-7900.

25. Garcia-Muñoz J.L., Suaaidi M., Martinez-lope M.J., and Alonso J.A., Room temperature Mott metal-insulator transition and its systematic control in  $\text{Sm}_{1-x}\text{Ca}_x\text{NiO}_3$  thin films, *Physical Review B*, 1995, 52, 13563-13569.
26. Alonso J.A., Martinez-Lope M.J., Hidalgo M.A., Metal-Insulator Transition and Magnetic Properties of  $\text{La}_{1-x}\text{Eu}_x\text{NiO}_3$  ( $x=0-1.0$ ), *Journal of Solid State Chemistry*, 1995, 116, 146-156.
27. Chandra M., Das S., Aziz F., Tripathi S., Mavani K.R., Large effects of epitaxial tensile strain on electronic transport of Mn-doped  $\text{NdNiO}_3$  thin films, *Solid State Communication*, 2015, 219, 16-20.
28. Alvarez I., Veiga M.L., Pico C., Metal-Insulator Transitions Induced by Doping in  $\text{LaNiO}_3$ :  $\text{LaNi}_{0.95}\text{M}_{0.05}\text{O}_3$  ( $M = \text{Mo}, \text{W}, \text{Sb}, \text{Ti}, \text{Cu}, \text{Zn}$ ) Perovskites, *Journal of Solid State Chemistry*, 1998, 136, 313-319.
29. Yadav E., Harishankar S., Chandra M., Rajput P., Mavani K.R., Influence of Cu-doping and Thickness on metallic conductance in  $\text{PrNiO}_3$  thin films, *Applied Physics A.*, 2018, 124, 614.
30. Venimadhav A., Chaitanya Lekshmi I., Hedge M. S., Strain-induced metallic behaviour in  $\text{PrNiO}_3$  epitaxial thin films, *Material Research Bulletin*, 2002, 37, 201-8.
31. Ni induced few-layer graphene growth at low temperature by pulsed laser deposition: *AIP Advances*: Vol 1, No 2.
32. Boyd I. W., Thin film growth by pulsed laser deposition, *Ceramics International*, 1996, 22, 429-34.
33. Pulse Laser Deposition (PLD) – A Versatile Thin Film Technique, *ResearchGate*.
34. Landě A., The Physical Significance of Reciprocal Lattice of Crystals, Selected Scientific Papers of Alfred Landě Fundamental Theories of Physics (*Springer, Dordrecht*) pp 379-81.
35. High-Resolution X-Ray Scattering-From Thin Films to Lateral Nanostructures (*Ullrich Pietsch*) Springer.
36. Four-Point Probe Method, *Wikipedia*.

37. Resistivity by Four Probe Method: Solid State Physics Virtual Lab: Physical Sciences: Amrita Vishwa Vidhyapeetham Virtual Lab.
38. Agarwal Umesh P., Atalla Rajai H., Raman Spectroscopy, *ResearchGate*, 1995, 8, 152-181
39. Ferraro John R., Introductory Raman Spectroscopy, 2003, edition 2.
40. Ewen Smith, Geoffrey Dent, Modern Raman Spectroscopy: A Practical Approach, 2001, edition 2.
41. Sano K., Sasaki T., Yoneyama N., and Kobayashi N., Electron localization near the Mott-transition in the organic superconductor  $\kappa$ -(BEDT-TTF)<sub>2</sub>Cu[N(CN)<sub>2</sub>]Br, *Physical Review Letter*, 2010, 104, 217003.
42. Middey S., Chakhalian J., Mahadevan P., Freeland J.W., Millis A. J., and Sarma D., Physics of Ultrathin Films and Heterostructures of Rare-Earth Nickelates, *Annual Review Material Research*, 2016, 46, 205-34.
43. Vucicevic J., Tanaskovic D., Rozenberg M.J., Dobrosavljevic V., *Physical Review Letter*, (2015), 114, 246402.
44. Mikheev E., Hauser A.J., Himmetoglu B., Moreno N.E., Jannotti A., Bad-Metal Behaviour Reveals Mott Quabtum Critically In Doped Hubbard Model, Van de walle C.G., Stemmer S., *Science Advances*, (2015),.
45. Weber M.C., Guennou M., Dix N., Pesquera D., Sanchez F., Herranz G., Fontcuberta J., Lopez-Conesa L., Estrade S., Peiro F., Iniguez J., Kreisel J., Mutiple Strain-induced phase transitions in LaNiO<sub>3</sub> thin films, *Physical Review B*, (2016), 94, 014118.
46. Kumar Y., Bhatt H., Prajapat C.L., Basu S., Singh S., Interface Induced Magnetic Properties of Gd/Co Hetrostructures, *Journal of Applied Physics*, (2018), 124, 065302.
47. Gou G., Grinberg I., Rappe A.M., Rondinelli J.M., Lattice normal modes and electronic properties of the correlated metal LaNiO<sub>3</sub>, *Physical review B*, (2011), 84, 144101-1 – 144101-13.
48. Chaban N., Weber M., Pignard S., Kreisel J., Phonon Raman Scattering of perovskite LaNiO<sub>3</sub> thin films, *Applied Physics*, (2010), 97, 031915.

49. Soni K., Yadav E., Harisankar S., Mavani K.R., Influence of Ce doping and thickness on the structure and non-Fermi liquid behaviour of  $\text{LaNiO}_3$  thin films, *Journal of Physics And Chemistry of Solids*, (2020), 141, 109398